Precambrian Research 379 (2022) 106813

Contents lists available at ScienceDirect

Precambrian Research

journal homepage: www.elsevier.com/locate/precamres

Evolution of the Gállojávri ultramafic intrusion from U-Pb zircon ages and Rb-Sr, Sm-Nd and Lu-Hf isotope systematics

Alf Andre Orvik [a,*], Trond Slagstad [b], Bjørn Eske Sørensen [a], Ian Millar [c], Harald Hansen [d]

[a] Department of Geoscience and Petroleum, Norwegian University of Science and Technology, S. P. Andersens veg 15, 7031 Trondheim, Norway
[b] Geological Survey of Norway, Leiv Eirikssons vei 39, 7040 Trondheim, Norway
[c] Geochronology and Tracers Facility, British Geological Survey, Keyworth, Nottingham NG12 5GG, UK
[d] Department of Geosciences, UiT The Arctic University of Norway, Dramsveien 201, 9037 Tromsø, Norway

ARTICLE INFO

Keywords:
Crustal contamination
Karasjok Greenstone Belt
Magma conduit
Rb-Sr isotopes
Sm-Nd isotopes
zircon Hf

ABSTRACT

The Karasjok–Central Lapland Greenstone Belt is one of the largest Palaeoproterozoic greenstone belts in the Fennoscandian Shield and includes multiple (ultra)mafic intrusions, some with notable ore reserves, formed during three episodes at 2.44, 2.22 and 2.05 Ga. This study presents new mineralogical, geochronological and isotopic data for the Gállojávri ultramafic intrusion, in the Karasjok Greenstone Belt, northern Norway. Previous petrogenetic modelling suggests that the intrusion was emplaced as a conduit system open for influx of melt with signs of polybaric fractionation and assimilation. Zircon U-Pb geochronology yields an age of 2051 ± 8 Ma, interpreted to reflect magmatic crystallisation. Large variations in isotopic signature over decimetres to metres indicate incomplete magma mixing. In bulk samples, εNd(t) ranges from −15 to 4. Zircon εHf(t) ranges from −14 to −1. Bulk $^{87}Sr/^{86}Sr(t)$ shows an apparent range from 0.5041 to 0.7072: the anomalously low values and general alteration indicates that $^{87}Sr/^{86}Sr$ is non-primary, whereas the less mobile Sm-Nd/ Lu-Hf systems are interpreted to represent primary magmatic signatures. We ascribe the large variations in the Nd and Hf isotopic signatures to local melting or dissolution of xenoliths and influx of variably contaminated melt into the semi-consolidated Gállojávri magma chamber, consistent with a conduit model involving variable replenishment and crustal interaction. The most evolved isotopic signatures cannot be accounted for by interaction with the local Archaean basement, indicating the presence of unidentified crustal components at depth. The Gállojávri intrusion shows many petrogenetic similarities to other c. 2.05 Ga (ultra)mafic intrusions in the Central Lapland Greenstone Belt.

1. Introduction

Magmatic plumbing systems represent highly dynamic environments that often involve complicated multistage and polybaric evolutionary histories. The compositional variations observed in lavas and related subvolcanic cumulates reflect the complex interplay between physical and chemical processes during magma generation, differentiation and assimilation (Fowler et al., 2004; Orvik et al., 2022). For example, the transport of magmas through the continental lithosphere offers ample opportunities for thermal erosion and the subsequent addition of anatectic melt and country-rock residue to a magma body that leads to chemical contamination of a rock suite (Arndt and Jenner, 1986; Ding et al., 2012; Fowler et al., 2004). Crustally derived anatectic melts generally have distinctly different radiogenic and stable isotope ratios from mantle melts (Peate et al., 2008). Therefore, the addition of crustal melts can significantly modify the magma composition.

The chemical and isotopic effects of assimilation on melts that pass through the crustal column can provide important information about the local crustal architecture (Dickin and Durant, 2002; Peate et al., 2008). In addition, assimilation of country rock material is critical in generating magmatic Ni-Cu-(PGE) sulphide deposits (Ding et al., 2012; Lesher, 2017, 2019), with channelised sills, tubes or blade-shape dykes characterised by prolonged high-volume flow accounting for most of the known host igneous bodies to significant ore deposits worldwide (Barnes et al., 2016).

This contribution focuses on the Palaeoproterozic Gállojávri ultramafic intrusion in Arctic Norway that forms part of the Karasjok and Central Lapland Greenstone Belt (KCLGB), extending from Norway, through Finland, into Russia, and contains several types of (ultra)mafic plutonic bodies and coeval extrusive rocks (Fig. 1; Orvik et al., 2022). In

* Corresponding author.
E-mail address: alf.a.orvik@ntnu.no (A.A. Orvik).

https://doi.org/10.1016/j.precamres.2022.106813
Received 25 April 2022; Received in revised form 27 June 2022; Accepted 27 July 2022
Available online 5 August 2022

Finland, the (ultra)mafic plutonic bodies, some with notable ore reserves, are grouped into three intrusive episodes at 2.44, 2.22 and 2.05 Ga (Hanski and Huhma, 2005, and references therein). Previous geochronological and isotopic data are very few in the Karasjok area, inhibiting the correlation with the northern Norwegian intrusions.

The Gállojávri intrusion represents a mid-crustal magma conduit that funnelled coeval komatiites towards the surface. Previous thermodynamic modelling has revealed a complex multistage magmatic history, with magma injection(s), differentiation and assimilation at different levels in the crust (Orvik et al., 2022). However, variations in mineral and whole-rock geochemical composition forming the basis of the model are not well suited to constrain the nature of the wall rock material or melt recharges. To this end, we report new mineralogical, geochronological and isotopic data for the Gállojávri intrusion to test the current petrogenetic model and to correlate the intrusion to other KCLGB examples. The data reveal large variations in isotopic signatures, typically over small distances, that provide important information on the assembly of the intrusion and shed light on the crustal architecture beneath the Karasjok area.

2. Geological setting

The Gállojávri intrusion is located in the Karasjok Greenstone Belt (KGB), the northernmost extension of the Central Lapland Greenstone Belt (CLGB). Together, the KCLGB can be followed to Russian Karelia in the southeast, making it one of the largest Palaeoproterozoic greenstone belts in the Fennoscandian Shield (Fig. 1B; Moilanen et al., 2021). The KCLGB records a prolonged extensional regime (c. 2.45–1.92 Ga) with volcano-sedimentary deposits on top of Archaean basement (Hanski and Huhma, 2005), showing a gradual deepening of the rift-basin from subaerial and shallow-water conditions to deeper-water conditions (Hanski and Huhma, 2005; Moilanen et al., 2021).

The KGB rocks have been deformed and metamorphosed under greenschist- to amphibolite-facies conditions (Braathen and Davidsen, 2000) and nonconformably overlie and are partly thrusted over the tonalite-trondhjemite-granodiorite-granite (TTGG)-dominated Archaean Jergul Gneiss Complex to the west (Fig. 1B & 2A). The variably gneissic Jergul Gneiss Complex is of Karelian affinity and formed between c. 2.98 and 2.78 Ga (Bingen et al., 2015).

The lowest unit in the KGB lithostratigraphy is the Lavtevárri formation consisting of a basal conglomerate underlying fine-grained foliated amphibolites, metapelites and metakomatiites (Fig. 2B; Braathen and Davidsen, 2000). The overlying Čorgaš formation has a lower portion of conglomerates, psammites and metapelites and an upper section of shallow-marine sedimentary rocks and subaerial to shallow-water mafic volcanic rocks (Fig. 2C; Barnes and Often, 1990; Braathen and Davidsen, 2000; Stokmo, 2020).

The basal contact of the Brittágielas formation with the underlying Čorgaš formation consists of an extensive marble unit (Fig. 2D; Braathen and Davidsen, 2000). The lower part of the Brittágielás formation

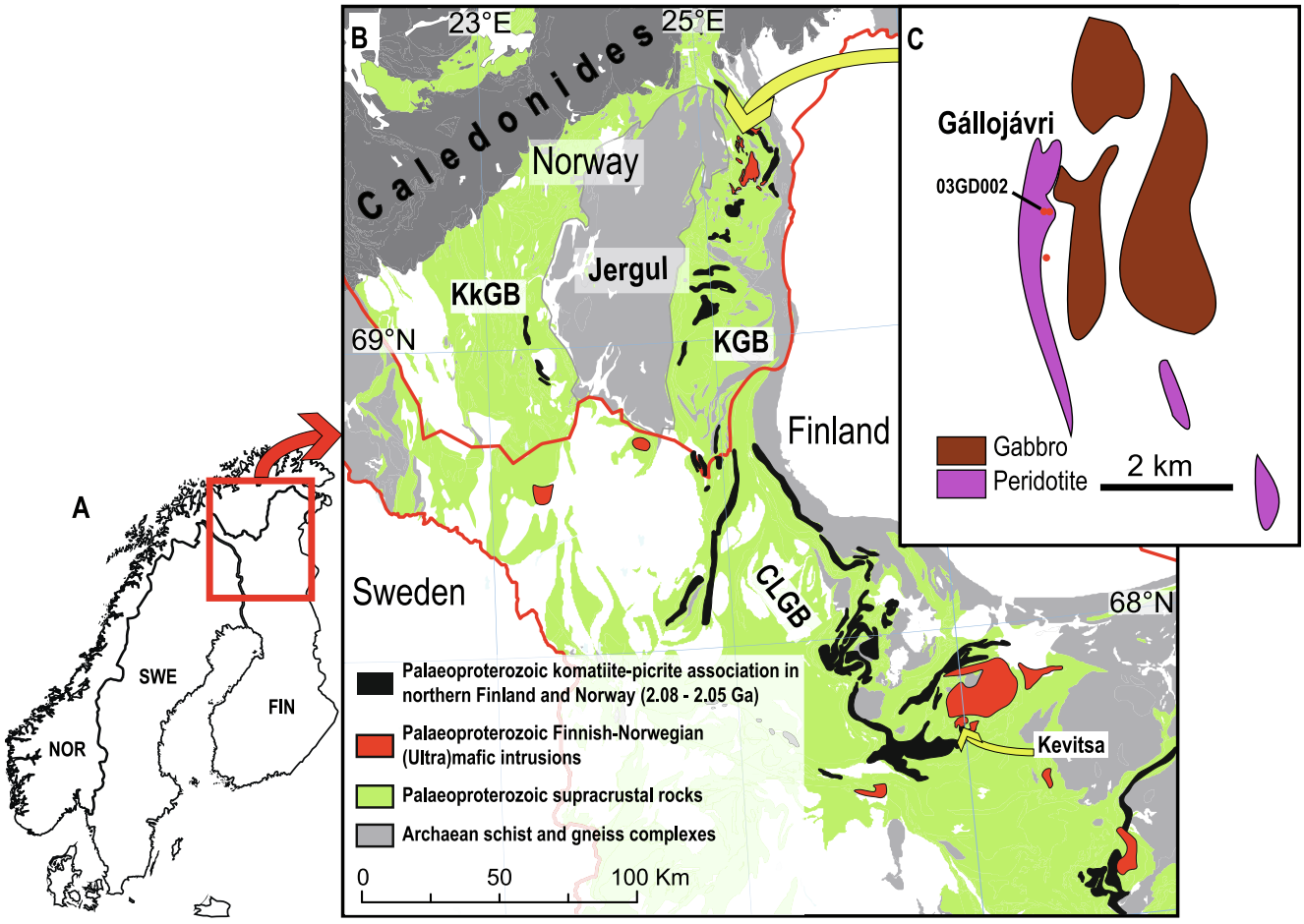

Fig. 1. (A) Sketch map of Scandinavia. The red box shows the location of the geological map in (B). (B) Simplified geological map showing the extension of the greenstone belt and distribution of Palaeoproterozoic (ultra)mafic extrusive and intrusive rocks. The map is modified from Orvik et al. (2022), Bingen et al. (2015), Hanski et al. (2001), Hanski and Huhma (2005), Puchtel et al. (2020), and based on Koistinen et al. (2001). (C) Sketch map of the Gállojávri ultramafic intrusion and adjacent intrusive rocks modified from Henriksen (1986) with the location of drill hole 03GD002 and other holes intercepting the Gállojávri intrusion (red dots). Abbreviations: Norway (NOR), Sweden (SWE), Finland (FIN), Kautokeino Greenstone Belt (KkGB), Karasjok Greenstone Belt (KGB) and the Central Lapland Greenstone Belt (CLGB). (For interpretation of the references to colour in this figure legend, the reader is referred to the web version of this article.)

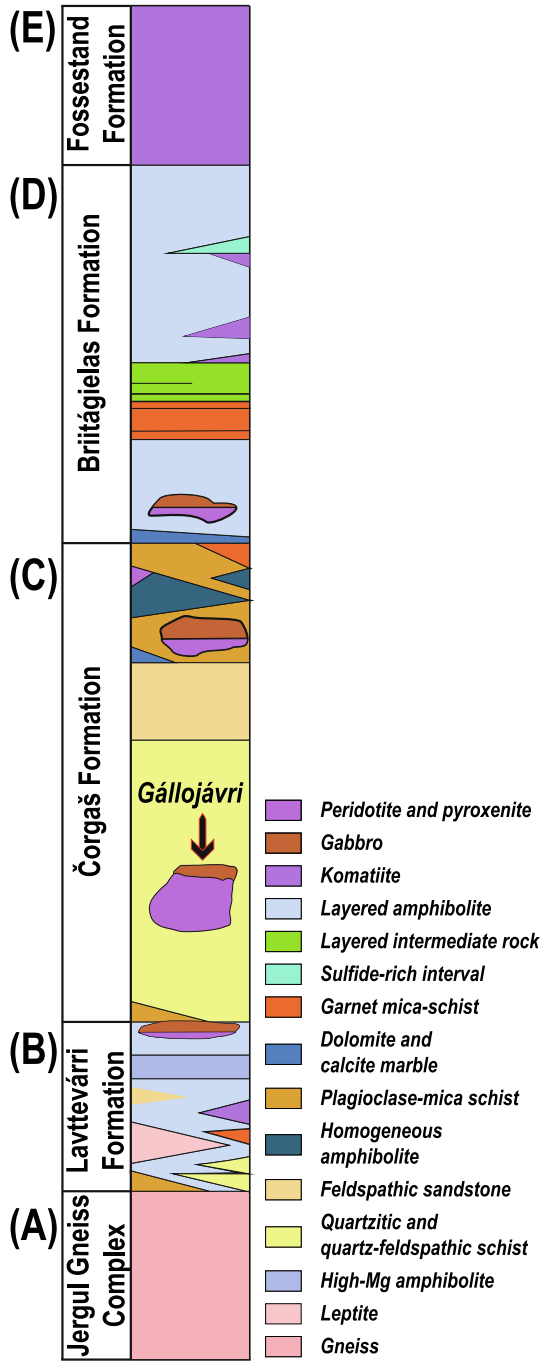

Fig. 2. The lithostratigraphy of the Karasjok Greenstone belt, modified from Orvik et al. (2022) and Hansen et al. (2020).

comprises calc-alkaline metavolcanic rocks and kyanite-bearing mica schists and an upper portion of layered amphibolites. Four 70 m-thick units of metakomatiite also distinguish the Brittágielas formation (Barnes and Often, 1990; Braathen and Davidsen, 2000). Metakomatiitic and volcanoclastic rocks dominate the upper Fossestrand formation (Fig. 2E; Stokmo, 2020). The lower portion comprises pillowed lavas that underlie lava flows and agglomerates. Mafic plutonic bodies have also been identified within the Fossestrand formation (Braathen and Davidsen, 2000).

Ultramafic to mafic intrusions are common in the Čorgaš formation. Several of these host Ni-Cu-PGE mineralisations and have drawn the interest of exploration companies, most notably the Karenhaugen-, Porsvann- and Gállojávri intrusions (Eilu, 2012). There are no published ages for these intrusions. However, carbon isotope chemostratigraphy on carbonates within the Čorgaš formation suggests a depositional age between c. 2.22 and 2.14 Ga (Melezhik et al., 2015). Bearing in mind that the (ultra)mafic intrusions of the KCLGB are interpreted to have formed in separate magmatic episodes at c. 2.44, 2.22 and 2.05 Ga (Hanski and Huhma, 2005), the maximum age provided by the isotope chemostratigraphy implies that the intrusions in the Čorgaš formation are part of the youngest group (Orvik et al., 2022).

3. The Gállojávri intrusion

The Gállojávri intrusion is a small and variably altered ultramafic body with a north-south elongation (Fig. 1C). The intrusion crops out over an area of about 2.3 km^2, but is likely larger, as observed in magnetic- and gravimetric anomaly maps (Skaar, 2014). The apparent magmatic differentiation observed in drill cores is concordant to semi-concordant with the surrounding foliation, implying a sill-like intrusion.

A petrogenetic model for the Gállojávri intrusion, based on whole-rock geochemistry, mineral chemistry and thermodynamic modelling, was presented by Orvik et al. (2022). Here, we restate some of the key aspects of the model. The reader is encouraged to consult the more extensive discussion in the original publication for further details.

The Gállojávri intrusion represents a mid-crustal magmatic body. It is part of a plumbing system that channelled komatiitic melts spatially (and temporally) associated with the Gállojávri intrusion towards the surface. Chemically, the cumulate rocks of the intrusion have high LREE/HREE and LREE/HFSE ratios and negative Nb-Ta anomalies, which suggest a significant contribution from LREE-enriched continental crust. Moreover, trace element indicators of crustal assimilation are uniform, implying that the assimilation occurred in a staging chamber. Thermobarometric estimates strengthen this interpretation with pressure estimates clustering at c. 400 MPa but extending towards c. 700 MPa.

The thermodynamic modelling demonstrated that the local Karasjok-type komatiite (Barnes and Often, 1990) is a likely parental melt analogue. The primitive komatiite first intruded the lower Archaean crust, where the melt fractionated and assimilated anatectic melt from its host rocks. In the second stage, the hybrid melt migrated to the middle crust and continued to fractionate and assimilate crustal material. The modelling revealed that the Gállojávri intrusion represents an open magmatic system requiring at least one recharge event to replicate the phase equilibria and thermobarometric estimates (Orvik et al., 2022).

4. Methods

4.1. Magma chamber simulator

The Magma Chamber Simulator (MCS; Bohrson et al., 2014) is an energy- and mass-constrained model that quantifies the phase, thermal and compositional evolution of a multiphase–multicomponent system of a fractionally crystallising resident magma body (melt + solid ± fluid), coupled with wall rock and multiple recharge reservoirs (Bohrson et al., 2020; Heinonen et al., 2020). The MCS uses the family of MELTS engines (Ghiorso and Gualda, 2015; Ghiorso et al., 2002; Ghiorso and Sack, 1995; Gualda et al., 2012) to quantify phase equilibria in the different subsystems separated by thermodynamic boundaries capable of transferring heat and mass (Bohrson et al., 2014; Heinonen et al., 2020). The phase equilibria of the magmatic subsystems at given P-T conditions are controlled by the major (±minor) element composition and the thermodynamic properties of the liquid + solid ± fluid phases present.

The MCS quantifies these parameters in an isobaric resident magma chamber. It evolves in temperature decrements while being open to the assimilation of anatectic melts and the influx of recharge melts. In the MCS, self-consistent thermodynamic modelling traces the thermal, mass and compositional evolution of the multicomponent–multiphase system

of the resident magma, wall rock and recharge reservoir by coupling the subsystems thermodynamic output with an executive Excel visual basic program (*MCS-PhaseEQ*; Bohrson et al., 2014). For more information on the use and design of the modelling tool, we refer to several articles introducing MCS (e.g., Bohrson et al., 2014; Bohrson et al., 2020; Heinonen et al., 2020; Heinonen et al., 2021; Heinonen et al., 2019) and the prior application to the Gállojávri intrusion (i.e., Orvik et al., 2022).

4.1.1. Magma chamber simulator: Trace elements and isotopes

In general, trace elements are too diluted to be primary stoichiometric constituents of magmatic phases and do not influence the phase equilibria (Hanson, 1989; Hanson and Langmuir, 1978). The distribution of trace elements is described by the partition coefficient (K_{sm}), which is the ratio of the concentration of an element in a solid phase versus the concentration in melt (Heinonen et al., 2020). In fractionating magmatic systems, multiple solid phases often crystallise simultaneously. In these cases, the bulk partition coefficient (D_{sm}) describes the chemical fractionation; that is, the sum of phase-specific K_{sm} scaled by the mass fraction of each solid phase.

Since trace elements are too dilute to influence phase equilibria, they are treated separately in MCS using the *MCS-Traces* tool (Bohrson et al., 2014). However, information on the composition and relative quantities of stable phases in magmatic systems are necessary to calculate D_{sm}. Therefore, the detailed modelling of trace elements (and isotopes) is impossible without recording major (±minor) element phase equilibria and mass fractions with the *MCS-PhaseEQ* tool. *MCS-Traces* uses the primary output of the *MCS-PhaseEQ* and reads it as the step-wise progression of the magmatic system (Bohrson et al., 2014; Heinonen et al., 2020). The *MCS-Traces* tool calculates isotopic ratios and trace element concentrations for each step defined in the primary *MCS-PhaseEQ* output. Additional input necessary to complete these calculations includes K_{sm} for each relevant phase and element and initial trace element concentrations and isotopic compositions for the melt and wall-rock reservoirs. The recharge reservoirs require only the initial trace element concentrations and isotopic ratios (Bohrson et al., 2014). For more information on the design and operational details of *MCS-Traces*, we refer to the introductory articles of Bohrson et al. (2014) and Heinonen et al. (2020).

4.2. Analytical methods

Thirteen samples selected from drill core 03GD002 (Fig. 1C; collar coordinates (DMS): N 69° 37′ 51.0672, E 25° 23′ 3.9948) were mineralogically characterised with X-ray Diffraction (XRD) and analysed for whole-rock Sr and Nd isotope compositions. Zircon from four of the 13 samples was prepared for in-situ U-Pb geochronology, trace element and Hf isotope characterisation. A detailed description of sample preparation and analytical methods is provided in Electronic supplement (ES) 1.

5. Sample petrography

Fig. 3 shows the CIPW normative mineralogy calculated from major element whole rock data (ES-2) and a simplified lithological log (Orvik et al., 2022). The labelled diamonds to the right in the figure give the locations of the samples analysed in this study. In cases where we can infer protolith lithology, we omit the prefix 'meta' for metamagmatic rocks, but note that all investigated rocks have been metamorphosed under greenschist and amphibolite facies and undergone variable low-temperature alteration.

The lower part of the drilled section consists of a coarse-grained and variably altered olivine-pyroxene cumulate unit. Sample *628*, located in the lower end (Fig. 3), is an orthocumulate with inequigranular olivine (c. 1–4 mm), orthopyroxene (c. 1–7 mm) and clinopyroxene (1–3 mm) (Fig. 4A). The olivine (c. 40–50 modal%) has a forsterite content of c. 81 % (Orvik et al., 2022) and is present as moderately serpentinised inclusions in the pyroxenes. Orthopyroxene (c. 20–30 %) is subhedral to anhedral, commonly with chaddacrysts of clinopyroxene, olivine and spinel

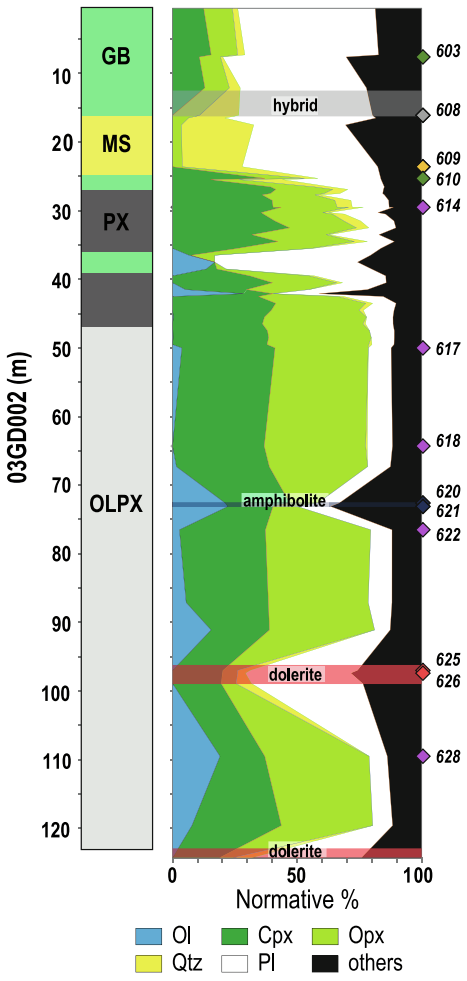

Fig. 3. Downhole CIPW normative mineralogy calculated from the major element whole-rock data of Orvik et al. (2022). Abbreviations: gabbro (GB), metasedimentary rocks (MS), pyroxenite (PX), olivine pyroxenite (OLPX), olivine (Ol), clinopyroxene (Cpx), orthopyroxene (Opx), quartz (Qtz) and plagioclase (Pl). The 'others' category includes normative hematite, orthoclase, sphene, corundum, pyrite, ilmenite, apatite, rutile, perovskite and nepheline.

(Fig. 4B). The clinopyroxene (10–20 %) is mostly interstitial and anhedral, but some examples of subhedral cumulus crystals exist (Fig. 4A). Additional interstitial minerals include primary amphibole and saussuritised plagioclase.

Sample *622* is located in the middle of the olivine-pyroxene unit (Fig. 3). The sample is strongly altered with uralised pyroxenes and serpentinised olivine, making any petrographic evaluation of modal mineralogy or primary features difficult (Fig. 4C). Relict minerals of olivine (1–3 mm) and orthopyroxene (1–2 mm) indicate a slightly finer grain size than in sample *628*. No relict clinopyroxene was observed in thin section and it is likely completely replaced by amphibole.

At the top of the olivine-pyroxene unit, sample *617* (Fig. 4D) represents a slightly altered mesocumulate of clinopyroxene (40–50 %), olivine (20–30 %) and orthopyroxene (10–20 %). Clinopyroxene has a variable grain size of 0.5–3 mm and is subhedral to anhedral. The smaller subhedral grains are present as chadacrysts in lager orthopyroxene. Olivine is inequigranular with grain sizes of 1.5–3.5 mm and is partly serpentinised, showing mesh texture. Orthopyroxene grains (1.0–3.5 mm) are subhedral to anhedral; the largest grains are typically poikilitic with clinopyroxene inclusions (Fig. 4D). Plagioclase is the main interstitial mineral together with accessory phlogopite.

Samples *620* and *621* were collected from two closely spaced zones (marked amphibolite in Fig. 3) because of elevated Zr concentrations of

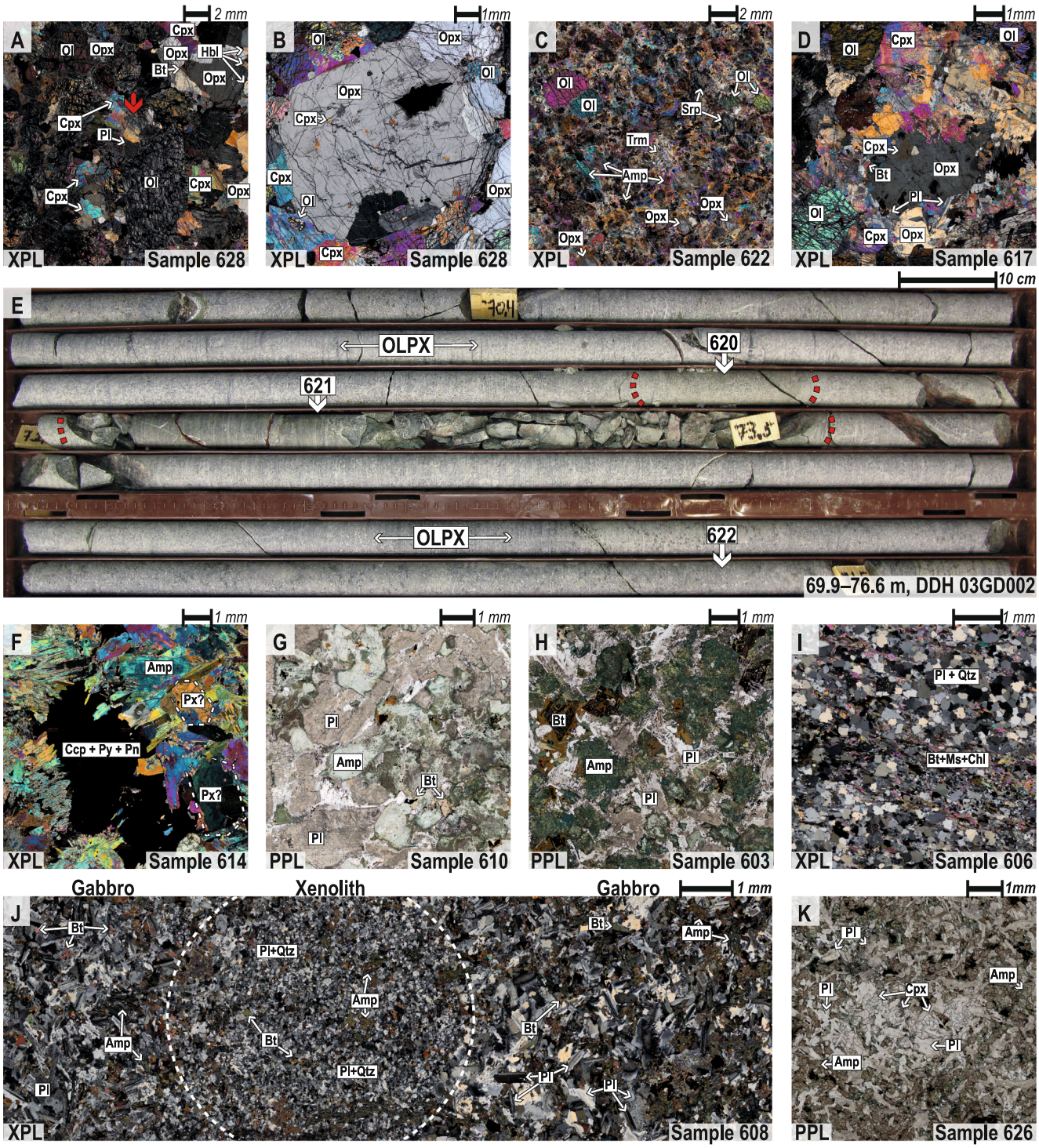

Fig. 4. Sample micrographs and images from this study. (A) Olivine-pyroxene orthocumulate. The red arrow points to subhedral cumulus clinopyroxene. (B) Large orthopyroxene with clinopyroxene chadacrysts. Note rounded olivine inclusion in interstitial clinopyroxene. (C) Extensively altered olivine-pyroxene cumulates with some relict olivine and orthopyroxene present. (D) Olivine-pyroxene mesocumulate with interstitial clinopyroxene and plagioclase. The orthopyroxene is poikilitic with chadacrysts of clinopyroxene. (E) Core section showing the location of samples 620 and 621. (F) Pyroxenite where secondary amphiboles completely replace the primary pyroxene. The stippled areas are thought to represent the relict outline of primary pyroxene. (G) Gabbro consisting of seriticized plagioclase, secondary amphibole and biotite. (H) Intergranular gabbro with partly seriticized plagioclase, secondary amphibole and sagenitic biotite. (I) Metasedimentary xenolith. (J) Hybrid intergranular gabbro with a rounded xenolith (outlined). (K) intergranular dolerite dyke. Abbreviations: cross-polarised light (XPL), plane-polarised light (PPL), olivine (Ol), orthopyroxene (Opx), clinopyroxene (Cpx), plagioclase (Pl), amphibole (Amp), tremolite (Trm), serpentine (Srp), chalcopyrite (Ccp), pyrite (Py), pentlandite (Pn), biotite (bt), quartz (Qtz), muscovite (Ms) and chlorite (Chl). (For interpretation of the references to colour in this figure legend, the reader is referred to the web version of this article.)

c. 150 ppm (ES-2; Orvik et al., 2022). These zones show gradual contact with the surrounding olivine pyroxenite unit and are extensively metasomatically altered (Fig. 4E), having 20–22 wt% MgO, 3.0–3.3 wt% K_2O and 152–165 ppm Rb. The samples are classified as amphibolites based on the XRD-determined mineralogy presented in the following section (Table 1). No thin sections were made from these sections because of the general alteration.

The coarse-grained olivine pyroxenite unit below grades into a medium-grained pyroxenite above (Fig. 3). The pyroxenites are characterised by a lack of normative olivine, disseminated sulphides and a near-complete replacement of primary silicate minerals by green amphibole, chlorite and biotite. In sample *614*, some relict pyroxene outlines indicate a grain size between 0.8 and 2.3 mm (Fig. 4F). Upward, the pyroxenites grade into gabbro with interstitial plagioclase. The plagioclase is largely replaced by saussurite, and the primary ferromagnesian minerals are completely replaced by green amphibole (Fig. 4G). The gabbro is less altered at the top of drill core 03GD002, with a primary intergranular texture. In sample *603* (Fig. 3), saussuritised plagioclase (30–40 %) laths 1–2 mm long enclose secondary amphibole, chlorite and sagenitic biotite (Fig. 4H).

Between c. 16 and 25 m, the drilled section consists of a xenolithic block of metasedimentary rock (Fig. 3). The section is dominated by plagioclase and quartz (60–80 modal%) with a grain size of c. 100–400 μm, with bands of chlorite, biotite, muscovite and amphibole (Fig. 4I).

Above the metasedimentary rocks, the gabbro is hybrid and contains minor, partly consumed xenoliths (Fig. 4J). The hybrid gabbro sample *608* is intergranular with partly saussuritised plagioclase (30–40 %) laths between 200 and 800 μm long. The granules consist of secondary amphibole, chlorite and biotite. The included xenoliths have transitional contacts with the surrounding gabbro and contain c. 70 % fine-grained (c. 50–150 μm) granoblastic plagioclase and quartz, the remaining being amphibole and biotite.

Dykes are common in all the drill cores (Orvik et al., 2022). Samples *625* and *626* were collected from a c. 4 m-thick dolerite sheet with sharp contacts. The dolerites have an intergranular texture with partly saussuritised plagioclase (30–40 %) measuring from 200 to 500 μm in length. The granules consist of c. 10 % clinopyroxene, c. 3 % ilmenite, and the remaining being secondary amphibole and chlorite (Fig. 4K).

6. Results

6.1. XRD-results

Table 1 shows the major phases identified with XRD (>1 wt%). The complete phase list and diffractograms are presented in ES-3. The magmatic lithologies have suffered moderate to severe alteration with secondary minerals (∑amphibole ± muscovite ± chlorite ± talc ± serpentine) in the range 11–98 wt% (Table 1).

6.2. Geochronology

Fig. 5 presents the U–Pb zircon geochronological data in Tera-Wasserburg diagrams. In Fig. 5A-D, the 2σ data-point error ellipses are colour scaled by the estimated common lead concentration. Electronic supplement 4 gives the complete dataset with cathodoluminescence (CL) images of zircon crystals. All ages are quoted with 2σ uncertainties.

Sample *609* is a metamorphosed feldspathic sandstone that hosts the Gállojávri intrusion. The sample comprise 48 % plagioclase, 31 % quartz, 7 % muscovite, 5 % biotite and 3 % diopside (Table 1). The zircon grains from this sample are c. 50–180 μm, anhedral and sub-rounded to stubby with aspect ratios between 1:1 and 3:1. The zircons are generally dark in CL, although some grains have cores with faint to strong oscillatory zoning suggesting a magmatic origin (ES-4). Other grains have dark and homogenous cores with CL-bright rims; however, core-mantle relationships are not ubiquitous. Some of the larger stubby to slightly elongated zircon grains show no apparent discontinuity between core and rim. Fifteen of the 24 analyses are >90 % concordant and have $^{207}Pb/^{206}Pb$ ages between 3022 ± 34 and 2652 ± 36 Ma. The majority (50 %) of the $^{207}Pb/^{206}Pb$ ages in concordant zircons are between 2845 ± 34 and 2746 ± 34 Ma. The discordant zircon analyses lie close to a discordia with an imprecise lower intercept of 528 ± 120 Ma (N = 24 & MSWD = 17; Fig. 5A), interpreted to reflect Caledonian lead loss.

Sample *603* is a coarse-grained intergranular gabbro, where secondary minerals largely replace the primary ferromagnesian minerals (Fig. 4H, Table 1). The zircon grains from this sample are c. 70–440 μm and subhedral. They are commonly needle-shaped acicular with aspect ratios up to 5:1 (ES-4). The highly elongated grains are characteristic of rapid growth (Corfu et al., 2003). The zircon grains are dark in CL, some with faint oscillatory or lengthwise zoning along the c-axis. Many of the grains have homogenous or mottled CL textures. There is significant variation in the U-Pb isotopic composition of the 24 analyses, and only two zircons have estimated common lead concentrations <0.5 %. The highest common lead concentrations are in grains with mottled or dark CL textures. Common lead is positively correlated with $(La/Sm)_N$ ($R \approx 0.8$), indicating metasomatic loss of Pb and gain in LREE. Calculating a discordia from 9 zircons with c. 1 % common lead or less gives upper and lower intercept ages of 2075 ± 16 and 368 ± 24 Ma (MSWD = 0.94), interpreted to reflect magmatic crystallisation and likely Caledonian Pb loss, respectively.

Sample *620* is an amphibolite where secondary minerals have entirely replaced the primary mineralogy (Table 1). The zircon grains from this sample are c. 80–240 μm, subhedral, stubby to prismatic with aspect ratios between 1:1 and 3:1. The zircons are dark in CL, some with faint oscillatory zoning (ES-4). Despite the general alteration of sample *620*, the zircon grains have lower estimated concentrations of common lead (<3.5 %) compared to sample *603*. Calculating a discordia based on

Table 1
Major phase XRD results (i.e. phase > 1 wt%) for samples analysed in this study. Lithological abbreviations: gabbro (GB), hybrid gabbro (HGB), metasediments (MS), ultramafic cumulate (UMC), amphibolite (AMP) and dolerite (DOL). Mineral abbreviations: quartz (Qz), plagioclase (Pl), olivine (Ol), diopside (Di), enstatite (En), biotite (bt), hornblende (Hb), kalifeldspar (Ksp), muscovite (Ms), chlorite (Chl), serpentine (Srp), magnetite (Mgt) and tremolite (Tr).

Sample	Depth (m)	Rock	Qz	Pl	Ol	Di	En	Bt	Hb	Ksp	Ms	Chl	Tlc	Srp	Mgt	Tr	Tot
603	7.6	GB	6	19		2		4	62	2		4					99
608	16.1	HGB	24	32		2		5	26			9					99
609	23.6	MS	31	48		3		5			7	5					99
610	25.3	GB	3	13		28	12	1	35			4	2				98
614	29.5	UMC							96	2		3					100
617	50	UMC			8	46	35		7		2			1			100
618	64.3	UMC										13			4	83	99
620	72.6	AMP						20	68			7	4				99
621	73.1	AMP						19	69			7	3		3		100
622	76.5	UMC			6		5					9		4	4	73	100
625	97	DOL	2	25		24			37	2	4	4					99
626	97.4	DOL		25		25			38	4	2	5					99
628	109.5	UMC			15	26	39		2		7			10			100

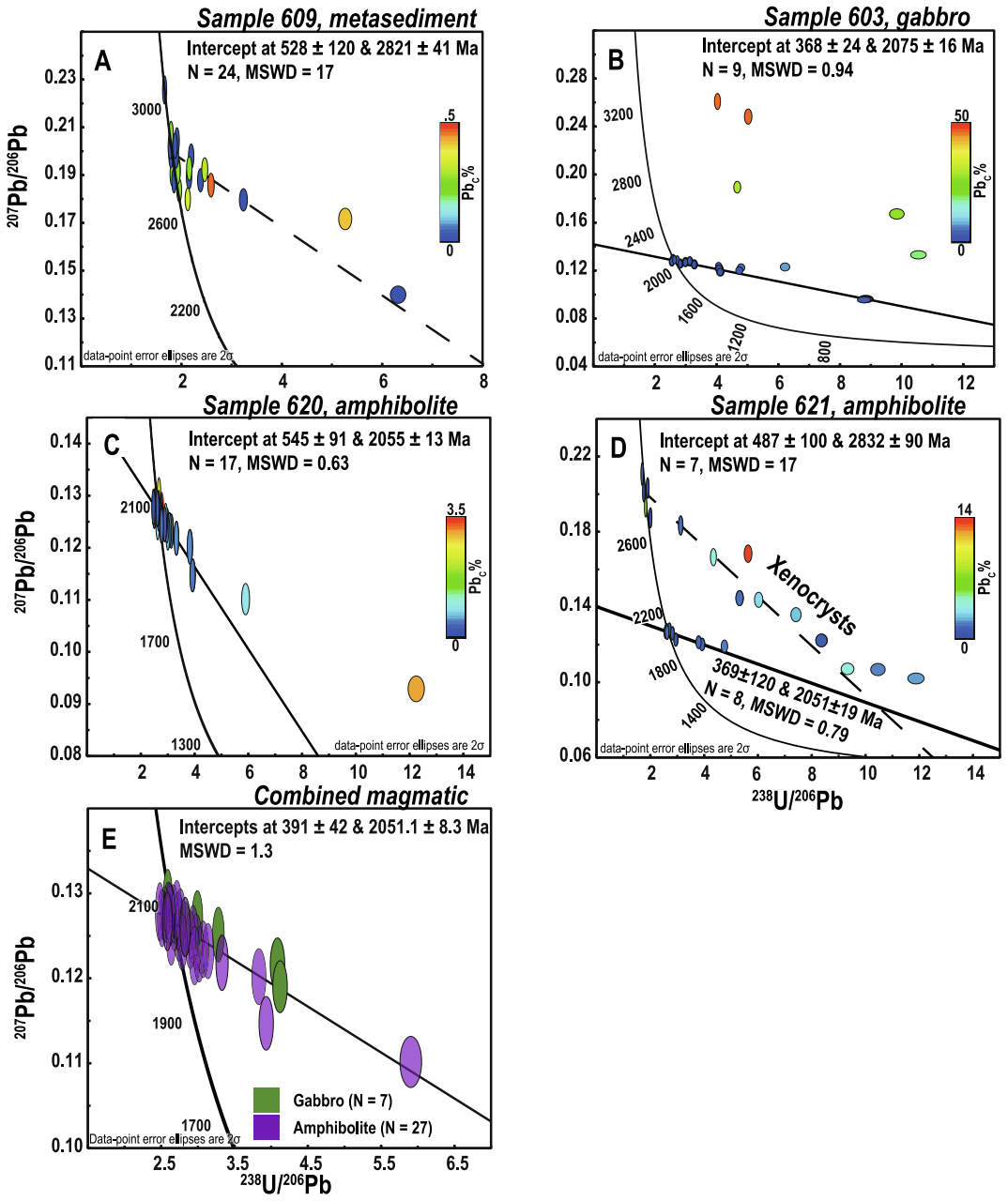

Fig. 5. U-Pb zircon geochronology. All the Tera-Wasserburg diagrams were created with Isoplot 4.15.11.10.15 using decay constants $\lambda_{238} = 1.55125 \times 10^{-10}$ and $\lambda_{235} = 9.8485 \times 10^{-10}$. (A) Metasediment wall-rock sample *609*. (B) Gabbro sample *603*. One outlier with 91 % common lead and a $^{207}Pb/^{206}Pb$ age of c. 5418 ± 30 Ma (i.e. *603–15*; ES-4) is omitted from the diagram. (C) Amphibolite sample *620*. (D) Amphibolite sample *621*. (E) shows a Tera-Wasserburg diagram with a discordia calculated by combining the magmatic zircon from the different samples.

24 analyses from 24 individual grains gives upper and lower intercept ages of 2041 ± 16 and 289 ± 33 Ma (MSWD = 2.8). The high MSWD indicates statistically significant deviation from linearity. Calculating a discordia based on 17 zircons with less than c. 1 % common lead gives upper and lower intercept ages of 2055 ± 13 and 545 ± 91 Ma (MSWD = 0.63; Fig. 5C), interpreted to reflect magmatic crystallisation and possibly Caledonian Pb loss, respectively.

Sample *621* is a amphibolite that resembles sample *620* chemically and mineralogically (Table 1). The primary mineralogy has been replaced entirely by secondary minerals. The zircon grains in this sample are c. 70–200 μm with aspect ratios between 1:1 and 3:1. The morphology of the zircon grains varies from anhedral to subhedral, subrounded or stubby to prismatic. The zircons are dark in CL, but some have brighter cores (ES-4). Some zircons are homogeneous and have faint oscillatory zoning from centre to rim, while others have rounded cores. Fig. 5D shows the 24 analyses from 23 zircon grains and shows that the sample contains two zircon populations. Regressing the individual populations of zircon with less than c. 1 % common lead gives one discordia with upper and lower intercept ages of 2832 ± 90 and 487 ± 100 Ma (MSWD = 17; N = 7) and another with upper and lower intercepts of 2051 ± 19 and 369 ± 120 Ma (MSWD = 0.79; N = 8). The lower intercepts are interpreted to reflect Caledonian Pb loss. The discordia with an upper intercept of 2832 ± 90 Ma is similar to the detrital zircon of sample *609*, indicating that these zircons are inherited. The high MSWD likely reflects the zircon grains' variable provenance (detrital). Only five xenocrystic zircons are > 90 % concordant with $^{207}Pb/^{206}Pb$ ages between 2912 ± 38 and 2720 ± 38 Ma. The discordia with an upper intercept age of 2051 ± 19 Ma is consistent with the

discordia ages of the magmatic zircons of sample *620* and *603* and likely reflect primary magmatic crystallisation.

The three U-Pb discordia ages from magmatic zircon range between 2051 ± 19 and 2055 ± 13 for the amphibolite samples and 2075 ± 16 Ma for the gabbro. The ages are statistically similar, and we cannot resolve a difference within a 2σ uncertainty. A combined regression of magmatic zircon analyses from all three samples with < 1 % common lead (N = 34) gives a well-defined discordia with upper and lower intercepts of 2051 ± 8 and 391 ± 42 Ma (MSWD = 1.3; Fig. 5E), taken here as the age of crystallisation of the Gállojávri intrusion.

6.3. Zircon Lu-Hf isotope data

Electronic supplement 5 presents the 55 in-situ Hf isotope analysis gathered from 54 zircon crystals selected from the four geochronology samples. Fourteen of the 55 analyses have propagated 2σ $^{176}Hf/^{177}Hf$ uncertainties above 5 ε-units and are therefore omitted from further reporting below. The initial epsilon Hf (εHf_t) is calculated relative to the upper intercept ages (c.f. Fig. 5). The εHf_t of xenocrystic and detrital zircon is calculated with the $^{207}Pb/^{206}Pb$ ages if < 10 % discordant; otherwise, initial values are relative to the upper intercept discordia age (2832 Ma) for xenocrystic zircon in sample *621*.

The nine zircon crystals analysed for Hf isotopes in the metasedimentary sample *609* show a range of εHf_t from −6.1 to 2.4, with a median value of 0.3 (Table 2). Except for the least radiogenic zircon, the values plot within the 3.0 and 3.5 Ga average crustal reference lines ($^{176}Lu/^{177}Lu = 0.015$) in the Hf isotope evolution plot (Fig. 6).

The ten xenocrystic zircons in sample *621* overlap with the detrital zircons of sample *609* in Fig. 6, with εHf_t from −3.6 to 4.6 and a median of 1.1 (Table 2). The four zircon grains from sample *621* interpreted to be magmatic have εHf_t from −14.4 to −10.0 and median of −10.6. These values overlap with sample *620*, which has εHf_t values from −11.5 to −8.2 and a median value of −10.2. As for sample *621*, it is noteworthy that these magmatic zircon grains indicate strong crustal involvement despite being collected from highly magnesian and LREE-depleted samples (see below).

The gabbroic sample *603* hosts the most radiogenic magmatic zircons identified in the Gállojávri intrusion (Table 2), although significant crustal involvement is still indicated by εHf_t from −7.5 to −1.4 with a median of −3.0 (Fig. 6). Two-stage depleted mantle model ages (T_{DM}) calculated relative to a depleted mantle model reservoir with present-day $^{176}Hf/^{177}Hf = 0.28325$ and $^{176}Lu/^{177}Hf = 0.0384$ and a crustal average $^{176}Lu/^{177}Hf = 0.015$ (Griffin et al., 2002; Griffin et al., 2000; Nowell et al., 1998) gives T_{DM} from c. 2.7 to 3.1 Ga, as opposed to zircons of the amphibolite samples giving model ages from c. 3.1 to 3.5 Ga.

6.4. Zircon trace element concentrations

Electronic supplement 6 presents the complete in-situ zircon trace element dataset. Although positively sloping, chondrite-normalised REE patterns characterise all samples, there is a relatively large variation between the samples and within a sample population. Therefore, we restrict further reporting on the trace element compositions to the 25 % and 75 % percentiles.

While overlapping in εHf_t and age in Fig. 6, the detrital- and xenocrystic zircon grains of samples *609* and *621* have distinctly different light- to middle-REE (L-/MREE) characteristics (Fig. 7A). Both zircon populations have positive Ce anomalies and similar $(La/Sm)_N$-ratios of 0.2–0.4 and 0.1–0.3 for *609* and *621*, respectively. However, the xenocrystic zircons of sample *621* have an order of magnitude higher LREE concentrations. The xenocrystic zircon is also distinguished by a positive Eu anomaly ranging from 1.2 to 7.4. A slightly negative Eu anomaly characterises the zircon of sample *609* (c. 0.6–1.1).

The magmatic zircons of samples *603*, *620* and *621* overlap in REE diagrams and are not easily distinguished (Fig. 7B). The magmatic zircons from sample *621* show the largest variation and are distinguished

Table 2
Summary of Lu-Hf isotope data.

Sample		Present-day $^{176}Hf/^{177}Hf$					εHf					T_{DM} (Ga)†				
	n	Min	1st quartile	Median	3rd quartile	Max	Min	1st quartile	Median	3rd quartile	Max	Min	1st quartile	Median	3rd quartile	Max
Metasediment																
609	9	0.28089	0.28096	0.28102	0.28105	0.28107	−6.1	−1.6	0.3	2.1	2.4	3.1	3.2	3.2	3.3	3.5
Gabbro																
603	10	0.28137	0.28146	0.28147	0.28149	0.28152	−7.5	−4.0	−3.0	−2.6	−1.4	2.7	2.8	2.8	2.9	3.1
Amphibolite																
620	8	0.28121	0.28121	0.28123	0.28126	0.28130	−11.5	−11.2	−10.2	−9.3	−8.2	3.1	3.2	3.3	3.3	3.3
621	4	0.28113	0.28116	0.28125	0.28126	0.28126	−14.4	−13.5	−10.6	−10.1	−10.0	3.2	3.2	3.3	3.4	3.5
Xenocrysts																
621	10	0.28091	0.28100	0.28107	0.28113	0.28120	−3.6	−0.7	1.1	3.2	4.6	3.0	3.1	3.2	3.3	3.5

† Two-stage depleted-mantle model ages (T_{DM}) were calculated relative to a depleted mantle model reservoir with present-day $^{176}Hf/^{177}Hf = 0.28325$ and $^{176}Lu/^{177}Hf = 0.0384$, and the crustal average $^{176}Lu/^{177}Hf = 0.015$ for the Hf isotope evolution of crustal magma sources after separation from the depleted mantle.

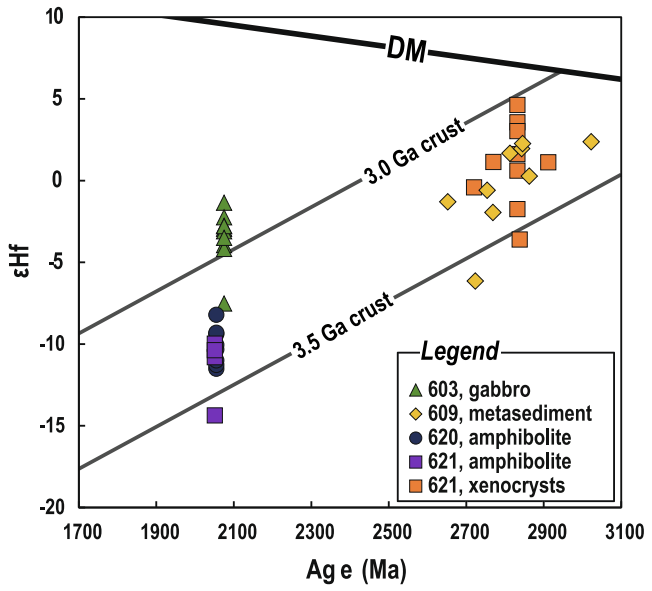

Fig. 6. Hf isotope evolution plot for the Gállojávri zircons. The isotope trajectories of the crust (formed at c. 2.9 and 3.5 Ga with $^{176}Lu/^{177}Lu = 0.015$) and depleted mantle (DM) are shown for reference.

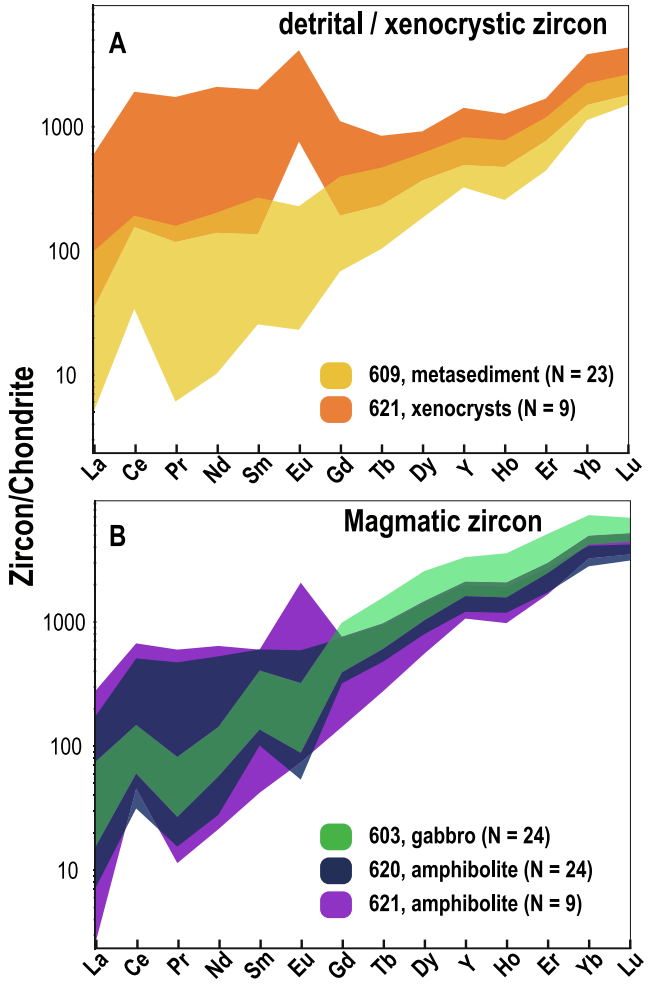

Fig. 7. Zircon trace element plots. (A) C1 chondrite normalised (Sun and McDonough, 1989) compositional fields (25 and 75% percentiles) for detrital and xenocrystic zircons. (B) C1 chondrite normalised fields for magmatic zircon.

by no to positive Eu anomalies (0.9–4.5); the other populations have negative Eu anomalies. The gabbroic zircons of sample *603* show the least variation with slightly higher heavy (H) REE concentrations.

6.5. Whole-rock Rb-Sr isotopes

The Rb-Sr isotope ratios are presented in Table 3 and Fig. 8. The initial Sr (Sr_i) compositions are calculated with a formation age of 2.05 Ga, except for the metasedimentary sample (*609*) calculated with the sample-specific zircon U-Pb age of 2.82 Ga (see Fig. 5A).

The hybrid gabbro (*608*) and metasedimentary rock (*609*) have the highest Sr_i compositions, with 0.70717 and 0.70709, respectively. There is considerable variation in Sr_i composition of the other magmatic rocks of the Gállojávri intrusion. The two gabbro samples range from 0.70002 (*610*) to 0.70477 (*603*). This range envelops the ultramafic cumulates with Sr_i from 0.70204 to 0.70413, excluding *618* that has Sr_i like the hybrid gabbro.

It is unlikely that sample *618* represents a closed system with respect to Sr as it is altered to a mineralogy dominated by tremolite and chlorite (Table 1). The two amphibolite samples (*620* and *621*) present clear evidence of Rb-Sr mobility with extremely high Rb concentrations (152, 165 ppm), present-day $^{87}Rb/^{86}Sr$ ranging from 27.1 to 28.2, and Sr_i initial ratios between 0.50410 and 0.57873; judging from mineralogy (Table 1), these values cannot represent primary magmatic ratios. The two dolerite samples also have unusually low Sr_i of 0.69192–0.69335, with mineral asseblages that indicates some alteration (Table 1). We note some uncertainty regarding the Sr_i of the dolerite dykes since we do not have a direct age. Regressing the magmatic whole-rock samples, excluding the hybrid gabbro, dolerite dykes and amphibolite sample *621* that contains abundant xenocrystic zircon, gives an errorchron age of 1691 ± 11 Ma (MSWD = 9) with a Sr_i of 0.7052 ± 0.0015 (Fig. 8). Despite the poor fit of the regression, the errorchron age might indicate when the Gállojávri Rb-Sr system was altered.

6.6. Whole-rock Sm-Nd isotopes

The whole-rock Sm-Nd isotope data are presented in Table 4 and Fig. 9, together with data compiled from the literature. As for Sr_i, all εNd_t values are calculated with a formation age of 2.05 Ga, except for the metasedimentary sample using the sample-specific zircon U-Pb age of 2.82 Ga. The compiled data presented in Fig. 9 have εNd_t calculated relative to the ages provided from the original references.

The magmatic whole-rock samples range about 19 ε-units, from −14.8 to 4.0 (Table 4). The ultramafic cumulates display the largest range from the most juvenile sample *622* ($\varepsilon Nd_t = 4.0$) to *617* with an εNd_t of −10.1. The εNd_t of sample *617* is less radiogenic than the extrapolated Nd isotope evolution trend of the metasedimentary sample (bold marked line in Fig. 9) and the exposed KGB Archaean basement, the Jergul Gneiss Complex (dark grey field; Fig. 9). The εNd_t of the two gabbro samples is consistent with the Sr isotopic data in that *610* is the most juvenile with an εNd_t of 2.5 and *603* being more evolved with an εNd_t of −1.4. The two dolerite samples have a narrow range close to that of sample *610,* with $\varepsilon Nd_t = 2.7–2.9$. The εNd_t of the hybrid gabbro (*608*) is −5.4, close to the Nd isotope evolution trend of the metasedimentary host rock (Fig. 9). There is an almost ten ε-unit difference between the two amphibolite samples, ranging from −14.8 to −5.0 for *620* and *621*, respectively. Sample *621* host a large amount of inherited zircon (see Fig. 5D) and plots close to the hybrid gabbro and the Nd evolution trend of the metasedimentary host rock (Fig. 9). Sample *620* has the most unradiogenic Nd composition of the dataset and plots well below the Nd isotope evolution trend of the local crystalline basement (Fig. 9).

6.7. Variation through the drill core

Fig. 10 shows the downhole variation in MgO wt.%, Nb/Th, εNd (2.05 Ga) and $^{87}Sr/^{86}Sr$ (2.05 Ga) in drill core 03GD002. Whole-rock

Table 3
Whole-rock Rb-Sr isotope data.

Sample no.	Rb (ppm)	Sr (ppm)	$^{87}Rb/^{86}Sr$	$^{87}Sr/^{86}Sr$	± 2σ	Age (Ma)	$^{87}Sr/^{86}Sr(t)$
Gabbro							
603	31.8	230	0.4005	0.716370	0.000008	2050	0.704768
610	26.8	109	0.7125	0.720658	0.000011	2050	0.700017
Hybrid gabbro							
608	49.5	289	0.4964	0.721547	0.000006	2050	0.707167
Dolerite							
625	46.1	174	0.7674	0.715577	0.000015	2050	0.693346
626	55	168.5	0.9458	0.719319	0.000014	2050	0.691921
Amphibolite							
620	165.5	18.8	27.1160	1.364232	0.000013	2050	0.578731
621	152.5	16.6	28.1838	1.320531	0.000016	2050	0.504099
Ultramafic cumulate							
614	2.6	13	0.5795	0.718823	0.000013	2050	0.702036
617	2.9	28.3	0.2967	0.710861	0.000009	2050	0.702267
618	1.7	19.7	0.2499	0.713758	0.000012	2050	0.706519
622	1	14.6	0.1983	0.709876	0.000013	2050	0.704132
628	3.2	22.2	0.4175	0.715386	0.000019	2050	0.703291
Metasediment							
609	63.4	298	0.6172	0.731825	0.000010	2821	0.707087

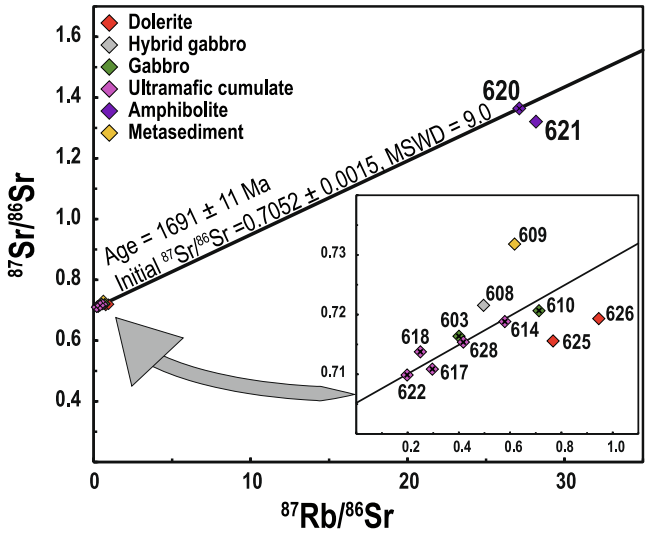

Fig. 8. Rb-Sr isochron diagram for whole-rock samples. For visibility, the lower-right isochron inset shows samples with $^{87}Rb/^{86}Sr < 1$. The errorchron (MSWD = 9.0) giving an age of 1691 ± 11 Ma and an initial $^{87}Sr/^{86}Sr$ of 0.7052 ± 0.0015 includes the eight samples marked with 'x'.

geochemistry for the samples in question is presented in ES-2, acquired from Orvik et al. (2022). From top to bottom in the drill core, the magmatic samples show increasing MgO (from 4 to 29 wt%) and uniformly low Nb/Th-ratios (c. 0.8–2.0). The low Nb/Th values are similar to the crustal average (~2.3; Weaver and Tarney, 1984) and may indicate significant contamination. The amphibolite and dolerite samples diverge from this generalisation (Fig. 10). The amphibolite samples (i.e. *620* and *621*) are texturally dissimilar from the surrounding ultramafic cumulate rocks but without distinct sharp boundaries. We note that the broken-up core makes definite contact relationships less clear (Fig. 4E). These samples have MgO in the range of 19–20 wt% and higher Nb/Th-values between 4.0 and 5.3. The dolerite samples are acquired from a fine-grained discontinuity (sheet) in the core and have MgO concentrations of c. 6 wt% with higher Nb/Th ratios in the range 5.5–6.0 (similar to primitive mantle Nb/Th ~ 8; Sun and McDonough, 1989).

The whole-rock isotopic data present a different and more complicated picture than the major- and trace elements (Fig. 10; c.f. Orvik et al., 2022). The large variation in Nd isotopic composition does not correlate with Nb/Th-ratios and shows erratic variation with depth. For example, the ultramafic cumulate samples have Nb/Th of 1.5 ± 0.3, suggesting uniform crustal contamination, but have εNd_t between −10.1 and +4 (Fig. 9). In the case of the dolerite samples, the positive εNd_t correlates with the highest Nb/Th ratios in the dataset. The amphibolite samples, however, also have high Nb/Th ratios but low to very low εNd_t values. In addition, the amphibolite samples and the most juvenile ultramafic cumulate sample (*622*) reveal highly localised variation in isotopic composition (Fig. 10). Fig. 4E shows the full range in Nd isotope composition within a core interval of c. 4 m.

7. Discussion

We interpret the upper intercept age of 2051 ± 8 Ma to correspond to crystallisation of the Gállojávri intrusion (Fig. 5E), similar to a geographically widespread c. 2.05 Ga group of (ultra)mafic intrusions and dykes in the Karelian province. In the Finnish CLGB, the c. 2.05 Ga group of layered intrusions locally cluster in the volcano-sedimentary Savukoski Group and consists of the 2063 ± 35 Ma Sakatti intrusion (re-Os isochron; Moilanen et al., 2021), the 2058 ± 4 Ma Kevitsa intrusion (U-Pb zircon; Mutanen and Huhma, 2001), the 2039 ± 14 Ma Moskuvaara intrusion (U-Pb zircon; Huhma et al., 2018), the 2035 ± 8 Ma Puijärvi gabbro and the 2025 ± 8 Ma Satovaara gabbro (average Pb-Pb; Huhma et al., 2018). If the Čorgaš formation-hosted Karenhaugen and Porsvann intrusions have similar ages to the Gállojávri intrusion, the c. 2.05 Ga (ultra)mafic intrusions likely extend throughout the KCLGB.

Considering Rb-Sr mobility, regional metamorphic history and the general alteration of the Gállojávri intrusion, the Rb-Sr isotope ratios are unlikely to represent primary magmatic ratios. The errorchron age of 1691 ± 11 Ma in Fig. 8 probably points to the timing of metamorphic overprinting and alteration and, although both age and significance remain speculative, we note that it broadly corresponds to hydrothermal activity, deformation and intrusion of pegmatite elsewhere in northern Fennoscandia (Bergh et al., 2015; Romer, 1996).

The two more immobile isotope systems (i.e., Lu-Hf and Sm-Nd) are more likely to represent primary magmatic ratios. The εHf_t magmatic zircon sample medians range from c. −11 to −3, with model ages between 2.8 and 3.3 Ga, implying a significant Archaean crustal contribution (Fig. 6). Crustal interaction is also evident from abundant xenocrystic zircon in sample *621* with Pb-Pb ages similar to the detrital zircon grains of sample *609*. Even larger variation is evident from the εNd_t data, ranging from depleted mantle values of c. 4 to strongly unradiogenic at c. −15. These findings align with the proposed multistage, polybaric petrogenetic model of the Gállojávri intrusion (Orvik et al., 2022). The large variation in εNd_t likely reflects the complexity of the evolution and the variable degree of interaction of the magmas with a continental crust of different ages and compositions. Furthermore, the

Table 4
Sm–Nd isotope data on whole rocks.

Sample no.	Sm (ppm)	Nd (ppm)	$^{147}Sm/^{144}Nd$	$^{143}Nd/^{144}Nd$	± 2σ	t (Ma)	εNd_t	T_{DM}(Ma)
Gabbro								
603	5.21	20.2	0.1559	0.512016	0.000005	2050	−1.4	2519
610	1.9	7.6	0.1511	0.512149	0.000007	2050	2.5	2068
Hybrid gabbro								
608	4.17	21.2	0.1189	0.511312	0.000004	2050	−5.4	2649
Dolerite								
625	3.06	11.2	0.1652	0.51235	0.000004	2050	2.7	2042
626	3.01	11.3	0.161	0.512305	0.000004	2050	2.9	2015
Amphibolite								
620	1.08	2.5	0.2612	0.512753	0.000007	2050	−14.8	
621	1.4	3.9	0.217	0.512658	0.000006	2050	−5	
Ultramafic cumulate								
614	0.98	3.3	0.1795	0.512346	0.000006	2050	−1.2	2740
617	0.86	2.4	0.2166	0.512394	0.000007	2050	−10.1	
618	0.91	2.6	0.2116	0.51251	0.000008	2050	−6.5	
622	0.54	2.1	0.1554	0.512284	0.000007	2050	4	1895
628	0.56	2.1	0.1612	0.51199	0.000007	2050	−3.3	2801
Metasediments								
609	4.61	29.8	0.0935	0.510908	0.000003	2821	3.8	2602

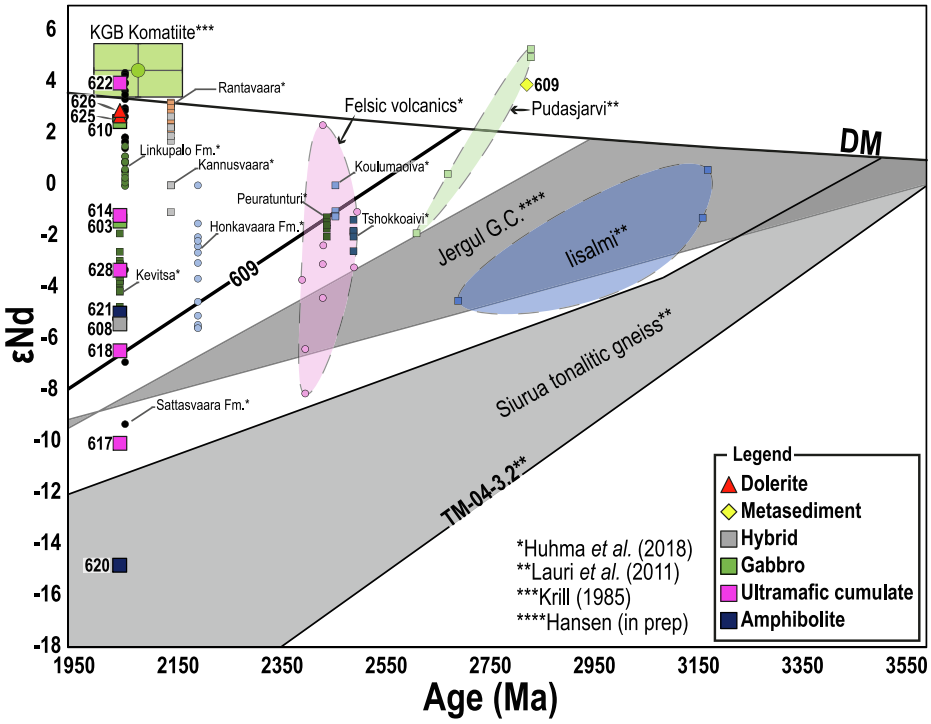

Fig. 9. Plot of εNd versus time for whole-rock samples of this study (identified in the legend) and compiled data from the Karelian province. Intrusions as squares, dykes as triangles and volcanic rocks as circles. The Palaeoproterozoic data from Linkupalo Fm., Kevitsa intrusion, Sattasvaara Fm., Rantavaara intrusion, Kannusvaara intrusion, Honkavaara Fm., felsic volcanic rocks (outlined), Peuratunturi intrusion, Koulumaoiva intrusion and the Tshokkoaivi intrusion were collected from the compilation of Huhma et al. (2018). Data for the Archaean Pudasjarvi (outlined) and Iisalmi (outlined) tonalite-trondhjemite-granodiorite-granite complexes and the Siurua tonalitic gneiss crustal evolution field are from Lauri et al. (2011). The shaded crustal evolution field of the Jergul Gneiss Complex (G.C.) is based on unpublished data (Hansen, in prep.). The Karasjok Greenstone Belt (KGB) komatiite average and 1σ error bars (green box) are based on data from Krill (1985). Depleted mantle (DM) evolution according to DePaolo (1981). (For interpretation of the references to colour in this figure legend, the reader is referred to the web version of this article.)

strongly unradiogenic Nd compositions documented for the ultramafic cumulate *617* ($\varepsilon Nd_t = -10.1$) and amphibolite *620* ($\varepsilon Nd_t = -14.8$) cannot be accounted for by interaction with local Archaean basement and indicate the presence of unidentified crustal components at depth (Fig. 9).

7.1. Testing the proposed petrogenetic model for the Gállojávri intrusion

The multistage (polybaric) recharge, assimilation and fractional crystallisation model of Orvik et al. (2022) used pillowed Karasjok-type komatiite (Barnes and Often, 1990) as the parental melt composition. In stage 1 of the model, the parental komatiite fractionated and interacted with crustal material at depth (700 MPa) represented by a weakly peraluminous normative granodiorite sample from the Jergul Gneiss Complex. The first simulation stage continued until the modelled melt had a composition similar to the chilled margin of the Gállojávri intrusion, represented by sample *610*. In stage 2 of the model, a melt with the composition of the chilled margin migrated to the middle crust (400 MPa), where it continued to fractionate and assimilate crustal material represented by the surrounding metasedimentary rocks. The stage 2 MCS simulation was constrained and tested by comparing the modelled solid and liquid phases with whole-rock and mineral chemistry. The modelling revealed that the system had to be open to recharge of melt to satisfactorily replicate the observed phase equilibria. Therefore, the second stage included the addition of juvenile komatiitic melt.

In the following, we implement the *MCS-PhaseEQ* models from Orvik et al. (2022) in *MCS-Traces* to test if the simulated variation in $^{87}Sr/^{86}Sr$ and $^{143}Nd/^{144}Nd$ is consistent with our reported ratios. We refer to the original paper for a detailed treatment of assumptions and choices of conditions and parameters. Table 5 gives the parental melt and wall rock composition used in the models. All isotopic ratios are back calculated to an age of 2.05 Ga.

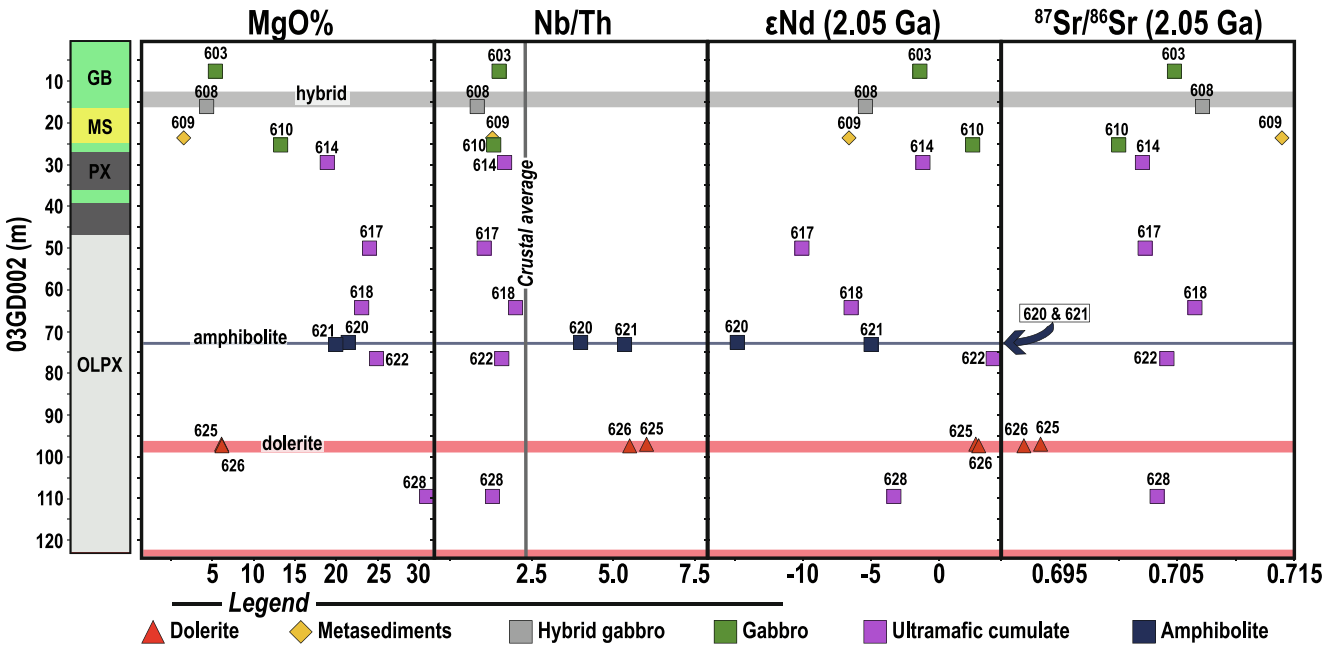

Fig. 10. Downhole variation in MgO wt.%, Nb/Th ratio, εNd (2.05 Ga) and $^{87}Sr/^{86}Sr$ (2.05 Ga) for drill core 03GD002. Crustal average Nb/Th from Weaver and Tarney (1984).

7.1.1. *MCS-Traces parameters*

Only sparse isotopic data exist for the KGB and the Archaean Jergul Gneiss Complex. Here, we use the average (N = 4) trace element composition and isotopic ratios of the 2085 ± 85 Ma (Sm-Nd error-chron) LREE depleted komatiite samples from Krill (1985) as the stage 1 parental melt and stage 2 recharge (Table 5). These samples are highly radiogenic with an εNd (2.05 Ga) of + 4.7, within error of expected depleted mantle values (Fig. 9; DePaolo, 1981). The initial wall rock parameters used for stages 1 and 2 of the isotope simulations are samples *041* and *103* (Table 5), collected from the Jergul Gneiss Complex (Hansen, in prep.) with crustal-like εNd (2.05 Ga) values of −8.7 and −8.6. The isotopic ratios of these samples were measured with the same methodology and instrumentation as in this study.

In the original *MCS-PhaseEQ* and trace element models, the stage 2 wall rock was assumed to be the metasedimentary host. Orvik et al. (2022) argued that the choice was somewhat arbitrary, as the Jergul Gneiss Complex samples and the metasedimentary host rocks are chemically similar. Indeed, the metasedimentary sample (*609*), a normative granodiorite, has an εNd (2.05 Ga) value of −6.6, making them hard to distinguish isotopically as well. Therefore, we use Jergul Gneiss Complex samples in both the lower- and middle crustal stages of the *MCS-Traces* simulation.

An irregularity in the original *MCS-PhaseEQ* model revealed by the isotopic data is that the assumed chilled margin (*610*) is too juvenile. The εNd (2.05 Ga) of + 2.5 is inconsistent with a melt that has experienced significant interaction with Archaean crustal material. Instead, in the stage 2 models, we use the modelled melt concentrations and isotopic ratios when the simulation has attained an MgO content of 12 wt%, like that of the previously assumed chilled margin.

The partition coefficients (K_{sm}) for both the resident magma body and wall-rock reservoirs are the same as in the original model. The values were collected from the EarthRef database (https://earthref.org/KDD/) and listed in the *MCS-Traces* output files provided in the supplementary material (Orvik et al., 2022, and references therein).

Table 5
Parental melt (PM), recharge (R) and wall rock (WR) compositions used in the models. Trace element concentrations in parts per million (ppm).

	Komatiite	041	103
	PM, R	WR	WR
Rb	0.1	114.5	62.4
Sr	55.9	134	248
Nd	2.9	31.3	12.9
Sm	1.1	5.8	3.29
$(^{87}Sr/^{86}Sr)_t$	0.702949	0.705622	0.714402
$(^{143}Nd/^{144}Nd)_t$	0.510225	0.509541	0.509545
εNd_t	4.7	−8.7	−8.6

Sources for the trace elements and isotope values are provided in the text. PM is the recharge magma composition in the stage 2 RAFC model. Initial isotope ratios calculated at 2.05 Ga.

7.1.2. *MCS-Traces results*

Fig. 11 shows the simulated variation in $^{143}Nd/^{144}Nd$ and $^{87}Sr/^{86}Sr$ compositions, together with most of the data from this study. The figure does not show the two amphibolite samples with $^{87}Sr/^{86}Sr$ (2.05 Ga) ratios between 0.50410 and 0.57873. The thick black lines in Fig. 11 reflect the two different wall-rock reservoirs. Electronic supplement 7 present the tabulated *MCS-Traces* output.

Most of the isotopic data match the simulated variation predicted by the *MCS-PhaseEQ* models (Fig. 11). Only a small amount of crustal contamination is needed to lower the $^{143}Nd/^{144}Nd$ composition initially, as the parental komatiite has a relatively low Nd concentration relative to the Jergul Gneiss Complex wall rocks and their partial melts. The rapidly decreasing $^{143}Nd/^{144}Nd$-ratio is especially apparent when the wall-rock reservoir has the composition of sample *041* with Nd = 31.3 ppm and $^{143}Nd/^{144}Nd$ (2.05 Ga) = 0.50954 (εNd_t = −8.7). In the model, the parental komatiitic melt, with a liquidus temperature of c. 1698 °C, intrudes the lower crust and after some heating of the wall rock, a 3 % addition of anatectic melt is needed to lower the $^{143}Nd/^{144}Nd$ from 0.51022 (εNd = +4.7) to 0.50994 (εNd = −0.8). When the parental melt has cooled to c. 1298 °C and has a composition consistent with the starting melt of the second-stage model, 15 % of anatectic crustal melt has been added, lowering the $^{143}Nd/^{144}Nd$-ratio of the melt in the resident magma chamber to 0.50967 (εNd = −6.1). The other assumed wall-rock reservoir, sample *103*, has a similar $^{143}Nd/^{144}Nd$-ratio, but because of the lower Nd concentration (12.9 ppm; Table 5), the simulation terminates with a $^{143}Nd/^{144}Nd$-ratio of 0.50980 (εNd = −3.7) after 15 % contamination (Fig. 11).

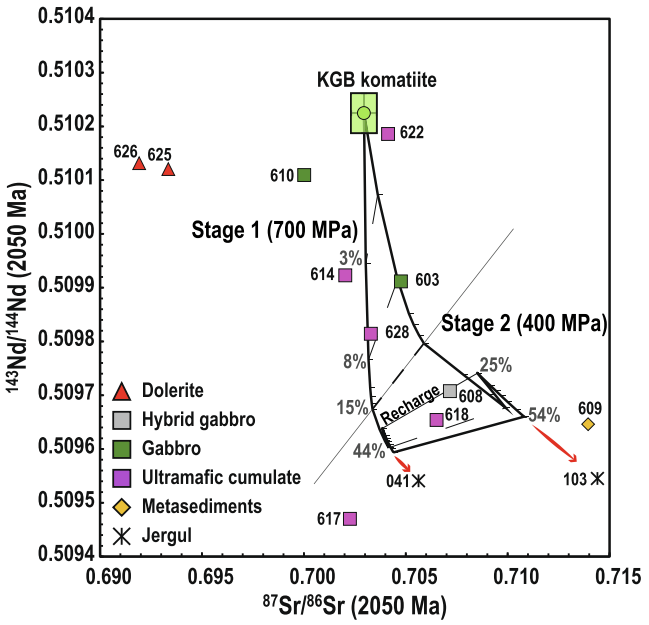

Fig. 11. Whole-rock Sr and Nd isotope ratio plot with the two-stage Magma Chamber Simulator models. The primary magma Sr and Nd isotope ratios for the stage 1 model are the averages of the LREE-depleted komatiite samples documented by Krill (1985).

In the second stage (400 MPa), the melt continues to fractionate and assimilate Jergul Gneiss Complex crustal material. When the melt in the resident magma chamber has cooled to c. 1026 °C, it has in total (stages 1 & 2) assimilated 44 % of anatectic melt and attained a slightly lower $^{143}Nd/^{144}Nd$ = 0.50960 (εNd = −7.5) when assimilating sample *041* (left; Fig. 11). At the same step in the model, using sample *103* to represent the wall-rock reservoir gives $^{143}Nd/^{144}Nd$ = 0.50968 (εNd = −6.0). The effects of contamination in the second stage are marginal compared to the first stage of the model. The hybrid resident melt has higher elemental concentrations and more similar isotopic ratios to the wall rock. Still, the variation predicted in the stage two simulations is consistent with our observations (Fig. 11).

In the original model by Orvik et al. (2022), a recharge of primitive komatiite is triggered at this step (at 1026 °C), adding a mass equivalent to 75 % of the starting resident melt mass. The relatively large mass only slightly increases the $^{143}Nd/^{144}Nd$ ratio of the melt in the resident chamber (Fig. 11). Although having a highly juvenile Nd isotope composition, the low Nd concentration of the recharge melt prevents it from significantly changing the resident melt composition.

The simulated compositional space follows similar trends but does not completely overlap with the available data. Inconsistencies include sample *610* with a Nd isotopic composition too juvenile to be consistent with a hybrid melt that has experienced significant crustal contamination. Sample *610* also plots off the trend of the other magmatic samples with a slightly lower $^{87}Sr/^{86}Sr$-ratio. It is also clear that our known wall-rock reservoirs cannot fully describe the observed variation. Both sample *617* and *620* are MgO-rich rocks with very low εNd values that require a more evolved crustal contaminant (Fig. 9).

8. Implications for crustal architecture, assembly of the Gállojávri intrusion, regional considerations and prospectivity

The Gállojávri intrusion exhibits a large variation in initial εNd, revealing the complexity of its composition, evolution and the variable degree of interaction of the parental magmas with crustal material. The isotopic variation is largely consistent with the previously suggested multistage and polybaric petrogenetic model of Orvik et al. (2022). Nevertheless, the lowest initial εNd values imply interaction with more evolved, unidentified continental crust in the KGB basement. This finding is not a complete surprise. In Finland, the Archaean basement of the western Karelian province contains compositionally diverse TTGGs formed between 3.5 and 2.8 Ga (Hölttä et al., 2012; Mutanen and Huhma, 2003). If the wall-rock reservoir had a composition similar to the c. 3.5 Ga Siurua tonalitic gneiss (Mutanen and Huhma, 2003), with an εNd (2.05 Ga) ~ −23 (Fig. 9; TM−04–3.2; Lauri et al., 2011), the first MCS model stage would result in a $^{143}Nd/^{144}Nd$ ratio of 0.50893 (εNd = −20.6; ES-8).

The simulated variation assumes complete mixing between the melt in the resident magma chamber and the added anatectic- and recharged melts. This assumption is unlikely to hold based on the downhole variation (Fig. 10) that shows large variations in isotopic signatures over very small distances (decimetres to a few metres). The heterogeneity implies incomplete mixing of isotopically distinct melts forming domains in the Gállojávri stratigraphy. A growing body of evidence suggests that several mid-to-upper crustal plutons are built by repeated injections into a crystal mush (Barboni et al., 2013; Bartley et al., 2008; Hepworth et al., 2020; Hepworth et al., 2017, 2018; Miller et al., 2011; Mungall et al., 2016; Nebel et al., 2020). For example, many of the major peridotite layers hosted in the Rum layered intrusion (NW Scotland) show lateral discontinuity, have upward-oriented apophyses and show cross-cutting relationships with the overlying troctolite, indicating that they formed via incremental sill emplacement (Hepworth et al., 2020; Hepworth et al., 2017, 2018). Geophysical imaging of active conduits has also revealed how the stacking of sills makes up part of smaller plumbing systems (Magee et al., 2018). For example, at various levels in the crust beneath the Afar depression (Ethiopia; Ebinger et al., 2008; Hammond, 2014), beneath the axis of the East Pacific Rise (Marjanović et al., 2014) and axial seamount in the northeastern Pacific Ocean (Carbotte et al., 2020). Also, high-precision U-Pb geochronology has led to the discovery of out-of-sequence layers in the Stillwater Complex (USA; Wall et al., 2018) and the Bushveld Complex (South Africa; Mungall et al., 2016). The zircon U-Pb geochronology recorded for the Gállojávri intrusion suggests an age difference between the younger isotopically evolved amphibolite samples and the older, more juvenile gabbro (Fig. 5). However, we are unable to resolve this with our current analytical precision.

In the case of the Gállojávri intrusion, the observed phase equilibria and the cumulate sequence can be satisfactorily replicated with thermodynamic modelling founded on classical ideas of magma chamber processes (Orvik et al., 2022). Therefore, we do not advocate a model where the random stacking of sills built the Gállojávri intrusion. However, this does not negate incomplete mixing with later magma injections, variable contamination by country rocks or local dissolution or melting of xenolithic blocks, which depends on rheological differences (e.g. Namur et al., 2015). If we exclude magma recharge, xenolith melting is the most efficient and quickest process leading to the hybridisation of a magmatic system (Robertson et al., 2015). It is also consistent with the presence of xenoliths in the hybrid zone (Fig. 4J) and the zircon xenocrysts distinguished in the U-Pb isotopic data (Fig. 5D). However, the lowest εNd values still require a crustal component different from what is documented in this study and suggest that some xenoliths derived from presently unexposed or unidentified crustal domains. The distance a xenolith can be transported would be contingent on the xenolith's lithology and the carrier magma's composition (McLeod and Sparks, 1998). If a xenolith is buoyant and takes a day to melt, the carrier magma could have flowed tens of kilometres (Barnes and Robertson, 2019).

Still, this does not explain the local juvenile isotope compositions observed in sample 622. Considering that most of the magmatic samples show signs of crustal interaction with an interquartile εNd range from −6.2 to −1.3, the local positive values suggest another mechanism leading to the juvenile domains. However, it is not uncommon for magmatic conduits to experience pulses of more primitive melt resulting in reverse compositional trends (Chistyakova and Latypov, 2012;

Latypov, 2015; Yudovskaya et al., 2015). This interpretation would be in-line with the MCS conduit model that requires recharge(s) of primitive, uncontaminated komatiite (Orvik et al., 2022).

We propose that the variability in the isotopic signature is the result of local dissolution or melting of xenoliths and incomplete mixing of late melt pulses injected into the hot and semi-consolidated Gállojávri chamber. We note that our interpretation is based on the variation observed in one drill core. To determine the spatial extent of the isotopically distinct domains would require a comprehensive drilling campaign and systematic sampling.

A possible KCLGB analogue is the contemporary Kevitsa Complex (c. 2.06 Ga; Mutanen and Huhma, 2001) that hosts an important Ni-Cu-PGE deposit. During the exploration and development of the Kevitsa mine (production began in 2012), the intrusion has benefited from multiple drilling campaigns (Santaguida et al., 2015). Luolavirta (2018), working with the extensive lithochemical database and drill cores, proposed a similar multistage and polybaric petrogenetic model. The intrusion represents a sub-volcanic conduit that, in the first stage, fed subaerial, contemporary picritic lavas (c. 2.06 Ga; Hanski et al., 2001). In the second stage, basaltic melt — fractionated in a staging magma chamber from the initial picrite, intruded through the same pre-established Kevitsa conduit (Luolavirta et al., 2018b, c). These stages resulted in a body of ultramafic cumulates that record a simple lithological stratigraphy with fairly constant $^{87}Sr/^{86}Sr$ compositions (Luolavirta, 2018; Luolavirta et al., 2018a; Luolavirta et al., 2018c) and average εNd (2.05 Ga) of -3.5 ± 0.5 (Huhma et al., 2018). The Ni-PGE ores hosted by the intrusion occur as irregular and discontinuous lens-like bodies (Yang et al., 2013). The ores are distinctly different to the surrounding cumulates, with complex internal architecture, cryptic variation and crustal isotopic signatures with high $^{87}Sr/^{86}Sr$ 0.709–0.711 (Luolavirta et al., 2018a) and low εNd −6.4 (Huhma et al., 2018). Luolavirta (2018) proposed a third stage of formation with repeated melt injections following a different route into the semi-consolidated Kevitsa magma chamber, which assimilated different and unidentified country-rock material and gave rise to the Ni-PGE ore (Luolavirta et al., 2018a; Luolavirta et al., 2018c).

The KCLGB contains numerous (ultra)mafic intrusive bodies and is considered highly prospective for Ni-Cu-(PGE) sulphides, with discoveries such as the Kevitsa and Sakatti deposits (Brownscombe et al., 2015). Orvik et al. (2022) noted that multiple injections of melt fractionated at various depths are probably widely applicable to the petrogenesis of Palaeoproterozoic Fennoscandian (ultra)mafic intrusions and a potentially effective mechanism for forming viable economic Ni-Cu-(PGE) deposits. In the Kevitsa intrusion, the high tenor Ni-PGE ores are interpreted to result from the assimilation of proto-ores (Mutanen, 1997; Yang et al., 2013), deposited with the ultramafic cumulates in the initial stages, by the repeated magma injections of the third stage (Luolavirta, 2018; Luolavirta et al., 2018a), similar to models proposed for ore mineralisations in Voisey's bay (Li and Naldrett, 1999), Noril'sk (Barnes and Lightfoot, 2005; Naldrett, 2004), Santa Rita (Barnes et al., 2011) and Kabanga (Maier and Barnes, 2010; Maier et al., 2010). The largest mafic layered intrusion on Earth, the Bushveld Complex in South Africa, contains significant quantities of Cr, Ni, V, Ti, Co and PGE. Despite the immense difference in size between the 2.3 km^2 Gállojávri intrusion and the ca. 60,000 km^2 Bushveld Complex, some tectonomagmatic aspects (plume related) and age (ca. 2050 Ma) appear to be similar (Cawthorn and Walraven, 1998; Scoates and Friedman, 2008). Several similarities also exist in terms of magmatic processes. In particular, the Bushveld Complex displays a range of isotopic compositions suggesting derivation from primitive mantle as well as enriched, subcontinental lithospheric sources, followed by variable interaction with lower cratonic crust and later by interaction with upper-crustal pelitic lithologies (e.g., Maier et al., 2000; Wilson et al., 2017). The existence of variably disaggregated xenolith of country rock also attest to interaction with the mafic magmas, with incomplete mixing and recharge of variably sourced and contaminated melts resulting in a lack of simple progressions in terms of magma evolution and stratigraphic control (Wilson et al., 2017). Studies of layered mafic intrusions invariably find evidence of extensive interaction with crustal rocks; however, although assimilation of S-rich rocks can be an important parameter for attaining sulphur saturation and, in turn, form a sulphide mineralization, the relationship between contamination and the formation of a deposit can be complex and in some cases dilute the metal tenors (Ihlenfeld and Keays, 2011).

This study and that of Orvik et al. (2022) have shown that the magmatic processes that operated in the Gállojávri intrusion are similar to those observed in similar, layered mafic intrusions of different age worldwide. In many cases, these intrusions carry significant occurrences of critical metals. Our work on the Gállojávri intrusion has provided new information about the magmatic evolution of the KGB and the composition of its Archaean substrate, and further work on the other ca. 2050 Ma mafic intrusions in the KGB, involving diamond drilling combined with petrographic, geochemical and isotopic studies, is likely to provide new information on the regional tectonomagmatic evolution and prospectivity of the region.

9. Conclusions

The data and modelling presented above lead to the following conclusions:

- Zircon U-Pb dating shows that the Gállojávri intrusion was emplaced at 2051 ± 8 Ma, suggesting it is part of a similarly aged group of (ultra)mafic intrusions in the KCLGB. Lower discordia intercept ages are consistent with Caledonian lead loss.
- The variation observed in the Sr–Nd–Hf isotopic data reveals the complexity of the magmatic evolution and aligns with the previously proposed multistage, polybaric petrogenetic model of the Gállojávri intrusion.
- The modelled isotopic variation is consistent with a previously proposed Karasjok-type komatiite parental magma; however, the strongly unradiogenic Nd compositions observed in ultramafic rocks suggest interaction with more evolved, unidentified crust in the KGB basement.
- Large variation in isotopic signatures over small distances suggests local dissolution or melting of xenoliths and incomplete mixing of isotopically distinct melts forming domains in the Gállojávri stratigraphy.

Funding

This research did not receive any specific grant from funding agencies in the public, commercial, or not-for-profit sectors. This study is part of Alf Andre Orvik's PhD Project on the Gállojávri intrusion in the Karasjok Greenstone Belt, funded by the Department of Geoscience and Petroleum, Faculty of Engineering, at the Norwegian University of Science and Technology and the Geological Survey of Norway. The Lu-Hf isotopic data were collected at the Norwegian Laboratory for Mineral and Materials Characterisation, MiMaC, for which the Research Council of Norway is acknowledged for support, project number 269842/F50.

CRediT authorship contribution statement

Alf Andre Orvik: Conceptualization, Investigation, Methodology, Data curation, Formal analysis, Writing – original draft. **Trond Slagstad:** Conceptualization, Investigation, Supervision, Data curation, Writing – review & editing. **Bjørn Eske Sørensen:** Data curation, Supervision, Writing – review & editing. **Ian Millar:** Investigation, Data curation, Writing – review & editing. **Harald Hansen:** Investigation, Resources, Writing – review & editing.

Declaration of Competing Interest

The authors declare that they have no known competing financial interests or personal relationships that could have appeared to influence the work reported in this paper.

Data availability statement

The data underlying this research are available in the article and in its online supplementary material.

Acknowledgements

We thank the reviewers and editor for constructive comments and suggestions that help clarify several aspects of the paper. We acknowledge the past drilling program by Tertiary Gold Ltd., which is a prerequisite for this study. We are grateful to Lars Petter Nilsson for sharing knowledge and providing insightful comments regarding the Gállojávri intrusion. We also want to acknowledge Doris Wagner and Nicola Atkinson at the British Geological Survey for their assistance with the Rb-Sr and Sm-Nd analysis.

Appendix A. Supplementary data

Supplementary data to this article can be found online at https://doi.org/10.1016/j.precamres.2022.106813.

References

Arndt, N.T., Jenner, G.A., 1986. Crustally contaminated komatiites and basalts from Kambalda, Western Australia. Chem. Geol. 56 (3-4), 229–255.
Barboni, M., Schoene, B., Ovtcharova, M., Bussy, F., Schaltegger, U., Gerdes, A., 2013. Timing of incremental pluton construction and magmatic activity in a back-arc setting revealed by ID-TIMS U/Pb and Hf isotopes on complex zircon grains. Chem. Geol. 342, 76–93.
Barnes, S.-J., Lightfoot, P.C., 2005. Formation of magmatic nickel-sulfide ore deposits and processses affecting their copper and platinum-group element contents. In: Hedenquist, J.W., Thompson, J.F.H., Goldfarb, R.J., Richards, J.P. (Eds.), One Hundredth Anniversary Volume. Society of Economic Geologists, Economic Geology, pp. 179–213. https://doi.org/10.5382/AV100.08.
Barnes, S.J., Cruden, A.R., Arndt, N., Saumur, B.M., 2016. The mineral system approach applied to magmatic Ni–Cu–PGE sulphide deposits. Ore Geol. Rev. 76, 296–316.
Barnes, S.-J., Often, M., 1990. Ti-Rich Komatiites from Northern Norway. Contrib. Miner. Petrol. 105 (1), 42–54.
Barnes, S.J., Osborne, G.A., Cook, D., Barnes, L., Maier, W.D., Godel, B., 2011. The Santa Rita Nickel Sulfide Deposit in the Fazenda Mirabela Intrusion, Bahia, Brazil: Geology, Sulfide Geochemistry, and Genesis. Econ. Geol. 106 (7), 1083–1110.
Barnes, S.J., Robertson, J.C., 2019. Time scales and length scales in magma flow pathways and the origin of magmatic Ni–Cu–PGE ore deposits. Geosci. Front. 10 (1), 77–87.
Bartley, J.M., Coleman, D.S., Glazner, A.F., 2008. Incremental pluton emplacement by magmatic crack-seal. Trans. Royal Soc. Edinburgh: Earth Sci. 97 (4), 383–396.
Bergh, S.G., Corfu, F., Priyatkina, N., Kullerud, K., Myhre, P.I., 2015. Multiple post-Svecofennian 1750–1560Ma pegmatite dykes in Archaean-Palaeoproterozoic rocks of the West Troms Basement Complex, North Norway: Geological significance and regional implications. Precambr. Res. 266, 425–439.
Bingen, B., Solli, A., Viola, G., Torgersen, E., Sandstad, J.S., Whitehouse, M.J., Røhr, T.S., Ganerød, M., Nasuti, A., 2015. Geochronology of the palaeoproterozoic kautokeino greenstone belt, finnmark, Norway: Tectonic implications in a Fennoscandia context. Norw. J. Geol. 95, 365–396.
Bohrson, W.A., Spera, F.J., Ghiorso, M.S., Brown, G.A., Creamer, J.B., Mayfield, A., 2014. Thermodynamic model for energy-constrained open-system evolution of crustal magma bodies undergoing simultaneous recharge, assimilation and crystallization: The magma chamber simulator. J. Petrol. 55, 1685–1717.
Bohrson, W.A., Spera, F.J., Heinonen, J.S., Brown, G.A., Scruggs, M.A., Adams, J.V., Takach, M.K., Zeff, G., Suikkanen, E., 2020. Diagnosing open-system magmatic processes using the Magma Chamber Simulator (MCS): part I—major elements and phase equilibria. Contrib. Miner. Petrol. 175, 1–29.
Braathen, A., Davidsen, B., 2000. Structure and stratigraphy of the Palaeoproterozoic Karasjok Greenstone Belt, north Norway - regional implications. Norw. J. Geol. 80 (1), 33–50.
Brownscombe, W., Ihlenfeld, C., Coppard, J., Hartshorne, C., Klatt, S., Siikaluoma, J.K., Herrington, R.J., 2015. The Sakatti Cu-Ni-PGE Sulfide Deposit in Northern Finland. In: Maier, W.D., Lahtinen, R., O'Brien, H. (Eds.), Mineral Deposits of Finland. Elsevier, pp. 211–252.
Carbotte, S.M., Arnulf, A., Spiegelman, M., Lee, M., Harding, A., Kent, G., Canales, J.P., Nedimović, M., 2020. Stacked sills forming a deep melt-mush feeder conduit beneath Axial Seamount. Geology 48, 693–697.
Cawthorn, R.G., Walraven, F., 1998. Emplacement and Crystallization Time for the Bushveld Complex. J. Petrol. 39 (9), 1669–1687.
Chistyakova, S., Latypov, R., 2012. Magma differentiation and crystallization in basaltic conduits by two competing petrogenetic processes. Lithos 148, 142–161.
Corfu, F., Hanchar, J.M., Hoskin, P.W., Kinny, P., 2003. Atlas of zircon textures. Rev. Mineral. Geochem. 53, 469–500.
DePaolo, D.J., 1981. Neodymium isotopes in the Colorado Front Range and crust–mantle evolution in the Proterozoic. Nature 291 (5812), 193–196.
Dickin, A.P., Durant, G.P., 2002. The Blackstones Bank igneous complex: geochemistry and crustal context of a submerged Tertiary igneous centre in the Scottish Hebrides. Geol. Mag. 139 (2), 199–207.
Ding, X., Ripley, E.M., Shirey, S.B., Li, C., 2012. Os, Nd, O and S isotope constraints on country rock contamination in the conduit-related Eagle Cu–Ni–(PGE) deposit, Midcontinent Rift System, Upper Michigan. Geochim. Cosmochim. Acta 89, 10–30.
Ebinger, C.J., Keir, D., Ayele, A., Calais, E., Wright, T.J., Belachew, M., Hammond, J.O.S., Campbell, E., Buck, W.R., 2008. Capturing magma intrusion and faulting processes during continental rupture: seismicity of the Dabbahu (Afar) rift. Geophys. J. Int. 174, 1138–1152.
Eilu, P., 2012. Mineral deposits and metallogeny of Fennoscandia. Geological Survey of Finland, Special Paper 53.
Fowler, S.J., Bohrson, W.A., Spera, F.J., 2004. Magmatic evolution of the Skye igneous centre, western Scotland: Modelling of assimilation, recharge and fractional crystallization. J. Petrol. 45, 2481–2505.
Ghiorso, M.S., Gualda, G.A.R., 2015. An H2O–CO2 mixed fluid saturation model compatible with rhyolite-MELTS. Contrib. Miner. Petrol. 169, 53.
Ghiorso, M.S., Hirschmann, M.M., Reiners, P.W., Kress, V.C., 2002. The pMELTS: A revision of MELTS for improved calculation of phase relations and major element partitioning related to partial melting of the mantle to 3 GPa. Geochem Geophy Geosy 3 (5), 1–35.
Ghiorso, M.S., Sack, R.O., 1995. Chemical mass transfer in magmatic processes IV. A revised and internally consistent thermodynamic model for the interpolation and extrapolation of liquid-solid equilibria in magmatic systems at elevated temperatures and pressures. Contrib. Miner. Petrol. 119 (2-3), 197–212.
Griffin, W.L., Pearson, N.J., Belousova, E., Jackson, S.E., van Achterbergh, E., O'Reilly, S. Y., Shee, S.R., 2000. The Hf isotope composition of cratonic mantle: LAM-MC-ICPMS analysis of zircon megacrysts in kimberlites. Geochim. Cosmochim. Acta 64 (1), 133–147.
Griffin, W.L., Wang, X., Jackson, S.E., Pearson, N.J., O'Reilly, S.Y., Xu, X., Zhou, X., 2002. Zircon chemistry and magma mixing, SE China: in-situ analysis of Hf isotopes, Tonglu and Pingtan igneous complexes. Lithos 61 (3-4), 237–269.
Gualda, G.A.R., Ghiorso, M.S., Lemons, R.V., Carley, T.L., 2012. Rhyolite-MELTS: a Modified Calibration of MELTS Optimized for Silica-rich, Fluid-bearing Magmatic Systems. J. Petrol. 53 (5), 875–890.
Hammond, J.O.S., 2014. Constraining melt geometries beneath the Afar Depression, Ethiopia from teleseismic receiver functions: The anisotropic H-k stacking technique. Geochem. Geophys. Geosyst. 15, 1316–1332.
Hansen, H., Slagstad, T., Bergh, S.G.. Geochemical volcanostratigrapy defines the tectonic evolution of the Karasjok Greenstone Belt, Finmark, The. https://doi.org/10.13140/RG.2.2.34380.16001.
Hanski, E., Huhma, H., 2005. Chapter 4 Central Lapland greenstone belt. In: Lehtinen, M., Nurmi, P.A., Rämö, O.T. (Eds.), Precambrian Geology of Finland Key to the Evolution of the Fennoscandian Shield. Elsevier, pp. 139–193. https://www.sciencedirect.com/science/article/abs/pii/S0166263505800052?via%3Dihub.
Hanski, E., Huhma, H., Rastas, P., Kamenetsky, V.S., 2001. The palaeoproterozoic komatiite-picrite association of Finnish lapland. J. Petrol. 42, 855–876.
Hanson, G.N., Langmuir, C.H., 1978. Modelling of major elements in mantle-melt systems using trace element approaches. Geochim. Cosmochim. Acta 42 (6), 725–741.
Hanson, G.N., 1989. An approach to trace element modeling using a simple igneous system as an example. In: Lipin, B.R., McKay, G.A. (Eds.), Geochemistry and Mineralogy of Rare Earth Elements. De Gruyter, p. 18. https://doi.org/10.1515/9781501509032-007.
Heinonen, J.S., Bohrson, W.A., Spera, F.J., Brown, G.A., Scruggs, M.A., Adams, J.V., 2020. Diagnosing open-system magmatic processes using the Magma Chamber Simulator (MCS): part II—trace elements and isotopes. Contrib. Miner. Petrol. 175, 1–21.
Heinonen, J.S., Luttinen, A.V., Spera, F.J., Bohrson, W.A., 2019. Deep open storage and shallow closed transport system for a continental flood basalt sequence revealed with Magma Chamber Simulator. Contributions to Mineralogy and Petrology 174, 87. https://doi.org/10.1007/s00410-019-1624-0.
Heinonen, J.S., Iles, K.A., Heinonen, A., Fred, R., Virtanen, V.J., Bohrson, W.A., Spera, F. J., 2021. From Binary Mixing to Magma Chamber Simulator: Geochemical Modeling of Assimilation in Magmatic Systems. In: Masotta, M., Beier, C., Mollo, S. (Eds.), Crustal Magmatic System Evolution, first ed. co-publication of the American Geophysical Union and John Wiley and Sons Inc, pp. 151–176.
Henriksen, H., 1986. Bedrock map Iddjajavri 2034 II M 1:50 000, preliminary edition. Geological Survey of Norway.
Hepworth, L.N., O'Driscoll, B., Gertisser, R., Daly, J.S., Emeleus, C.H., 2017. Incremental Construction of the Unit 10 Peridotite, Rum Eastern Layered Intrusion, NW Scotland. J. Petrol. 58, 137–166.
Hepworth, L.N., O'Driscoll, B., Gertisser, R., Daly, J.S., Emeleus, C.H., 2018. Linking In Situ Crystallization and Magma Replenishment via Sill Intrusion in the Rum Western Layered Intrusion, NW Scotland. J. Petrol. 59, 1605–1642.

Hepworth, L.N., Kaufmann, F.E.D., Hecht, L., Gertisser, R., O'Driscoll, B., 2020. Braided peridotite sills and metasomatism in the Rum Layered Suite, Scotland. Contributions Mineral. Petrol. 175, 17.
Huhma, H., Hanski, E., Kontinen, A., Vuollo, J., Mänttäri, I., Lahaye, Y., 2018. Sm–Nd and U-Pb isotope geochemistry of the Palaeoproterozoic mafic magmatism in eastern and northern Finland. Geological Survey of Finland. Bulletin 405, 150.
Ihlenfeld, C., Keays, R.R., 2011. Crustal contamination and PGE mineralization in the Platreef, Bushveld Complex, South Africa: evidence for multiple contamination events and transport of magmatic sulfides. Miner. Deposita 46, 813–832.
Hölttä, P., Heilimo, E., Huhma, H., Juopperi, H., Kontinen, A., Konnunaho, J., Sorjonen-Ward, P., 2012. Archaean complexes of the Karelia Province in Finland. *The Archaean of the Karelia Province in Finland*. Geological Survey of Finland, Espoo, Special Papers 54, 9–20.
Koistinen, T., Stephens, M., Bogatchev, V., Nordgulen, Ø., Wennerström, M., Korhonen, J., 2001. Geological map of the Fennoscandian Shield 1: 2 000 000. Espoo: Geological Survey of Finland, Trondheim: Geological Survey of Norway, Uppsala: Geological Survey of Sweden, Moscow: Ministry of Natural Resources of Russia. ISBN 951-690-812-8.
Krill, A.G., 1985. Rb-Sr, U-Pb and Sm-Nd isotopic dates from Precambrian rocks of Finnmark. Geological Survey of Norway Bulletin 403, 37–54.
Latypov, R., 2015. Basal Reversals in Mafic Sills and Layered Intrusions. In: Charlier, B., Namur, O., Latypov, R.M., Tegner, C. (Eds.), Layered Intrusions. Springer, Netherlands, pp. 259–293.
Lauri, L.S., Andersen, T., Hölttä, P., Huhma, H., Graham, S., 2011. Evolution of the Archaean Karelian Province in the Fennoscandian Shield in the light of U-Pb zircon ages and Sm-Nd and Lu-Hf isotope systematics. J. Geol. Soc. 168, 201–218.
Lesher, C.M., 2017. Roles of xenomelts, xenoliths, xenocrysts, xenovolatiles, residues, and skarns in the genesis, transport, and localization of magmatic Fe-Ni-Cu-PGE sulfides and chromite. Ore Geol. Rev. 90, 465–484.
Lesher, C.M., 2019. Up, down, or sideways: Emplacement of magmatic Fe–Ni–Cu–PGE sulfide melts in large igneous provinces. Can. J. Earth Sci. 56, 756–773.
Li, C., Naldrett, A.J., 1999. Geology and petrology of the Voisey's Bay intrusion: Reaction of olivine with sulfide and silicate liquids. Lithos 47, 1–31.
Luolavirta, K., 2018. Magmatic evolution of the Kevitsa igneous complex, northern Finland, and its relation to the associated Ni-Cu-(PGE) mineralization. University of Oulu, Res Terrae, p. 68.
Luolavirta, K., Hanski, E., Maier, W., Lahaye, Y., O'Brien, H., Santaguida, F., 2018a. In situ strontium and sulfur isotope investigation of the Ni-Cu-(PGE) sulfide ore-bearing Kevitsa intrusion, northern Finland. Miner. Deposita 53, 1019–1038.
Luolavirta, K., Hanski, E., Maier, W., Santaguida, F., 2018b. Characterization and origin of dunitic rocks in the NI-CU-(PGE) sulfide ore-bearing kevitsa intrusion, northern finland: Whole-rock and mineral chemical constraints. Bull. Geological Soci. Finland 90, 5–32.
Luolavirta, K., Hanski, E., Maier, W., Santaguida, F., 2018c. Whole-rock and mineral compositional constraints on the magmatic evolution of the Ni-Cu-(PGE) sulfide ore-bearing Kevitsa intrusion, northern Finland. Lithos 296–299, 37–53.
Magee, C., Stevenson, C.T.E., Ebmeier, S.K., Keir, D., Hammond, J.O.S., Gottsmann, J.H., Whaler, K.A., Schofield, N., Jackson, C.A.L., Petronis, M.S., O'Driscoll, B., Morgan, J., Cruden, A., Vollgger, S.A., Dering, G., Micklethwaite, S., Jackson, M.D., 2018. Magma Plumbing Systems: A Geophysical Perspective. J. Petrol. 59, 1217–1251.
Maier, W.D., Arndt, N.T., Curl, E.A., 2000. Progressive crustal contamination of the Bushveld Complex: evidence from Nd isotopic analyses of the cumulate rocks. Contrib. Miner. Petrol. 140, 316–327.
Maier, W.D., Barnes, S.-J., 2010. The Kabanga Ni sulfide deposits, Tanzania: II. Chalcophile and siderophile element geochemistry. Miner. Deposita 45, 443–460.
Maier, W.D., Barnes, S.J., Sarkar, A., Ripley, E., Li, C., Livesey, T., 2010. The Kabanga Ni sulfide deposit, Tanzania: I. Geology, petrography, silicate rock geochemistry, and sulfur and oxygen isotopes. Miner. Deposita 45, 419–441.
Marjanović, M., Carbotte, S.M., Carton, H., Nedimović, M.R., Mutter, J.C., Canales, J.P., 2014. A multi-sill magma plumbing system beneath the axis of the East Pacific Rise. Nat. Geosci. 7, 825–829.
McLeod, P., Sparks, R.S.J., 1998. The dynamics of xenolith assimilation. Contrib. Miner. Petrol. 132, 21–33.
Melezhik, V.A., Solli, A., Fallick, A.E., Davidsen, B., 2015. Chemostratigraphic constraints on the time of deposition of carbonate rocks in the Karasjok Greenstone Belt, northern Norway. Norw. J. Geol. 95, 299–314.
Miller, C.F., Furbish, D.J., Walker, B.A., Claiborne, L.L., Koteas, G.C., Bleick, H.A., Miller, J.S., 2011. Growth of plutons by incremental emplacement of sheets in crystal-rich host: Evidence from Miocene intrusions of the Colorado River region, Nevada, USA. Tectonophysics 500, 65–77.
Moilanen, M., Hanski, E., Yang, S.-H., 2021. Re-Os isotope geochemistry of the Palaeoproterozoic Sakatti Cu-Ni-PGE sulphide deposit in northern Finland. Ore Geol. Rev. 132, 104044.
Mungall, J.E., Kamo, S.L., McQuade, S., 2016. U-Pb geochronology documents out-of-sequence emplacement of ultramafic layers in the Bushveld Igneous Complex of South Africa. Nat. Commun. 7, 13385.
Mutanen, T., 1997. Geology and ore petrology of the Akanvaara and Koitelainen mafic layered intrusions and the Keivitsa-Satovaara layered complex, northern Finland. Geological Survey of Finland. Bulletin 395.
Mutanen, T., Huhma, H., 2001. U-Pb geochronology of the Koitelainen, Akanvaara and Keivitsa layered intrusions and related rocks. Geol. Surv. Finland Spec. Pap. 33, 229–246.
Mutanen, T., Huhma, H., 2003. The 3.5 Ga Siurua trondhjemite gneiss in the Archaean Pudasjarvi granulite belt, northern Finland. Bulletin-geological society of Finland 75, 51–68.
Naldrett, A.J., 2004. Magmatic Sulfide Deposits, 1 ed. Springer, Berlin, Heidelberg.
Namur, O., Abily, B., Boudreau, A.E., Blanchette, F., Bush, J.W.M., Ceuleneer, G., Charlier, B., Donaldson, C.H., Duchesne, J.-C., Higgins, M.D., Morata, D., Nielsen, T. F.D., O'Driscoll, B., Pang, K.N., Peacock, T., Spandler, C.J., Toramaru, A., Veksler, I. V., 2015. Igneous Layering in Basaltic Magma Chambers. In: Charlier, B., Namur, O., Latypov, R., Tegner, C. (Eds.), Layered Intrusions. Springer, Netherlands, pp. 75–152.
Nebel, O., Sossi, P.A., Ivanic, T.J., Benard, A., Gardiner, N.J., Langford, R.L., Arculus, R. J., 2020. Incremental Growth of Layered Mafic-Ultramafic Intrusions Through Melt Replenishment Into a Crystal Mush Zone Traced by Fe-Hf Isotope Systematics. Front. Earth Sci. 8, 1–10.
Nowell, G., Kempton, P., Noble, S., Fitton, J., Saunders, A., Mahoney, J., Taylor, R., 1998. High precision Hf isotope measurements of MORB and OIB by thermal ionisation mass spectrometry: insights into the depleted mantle. Chem. Geol. 149, 211–233.
Orvik, A.A., Slagstad, T., Hansen, H., Nilsson, L.P., Sørensen, B.E., 2022. The Palaeoproterozoic Gallujavri ultramafic intrusion, Karasjok Greenstone Belt; petrogenesis of a trans-crustal magma system. J. Petrol. 63, 28.
Peate, D.W., Barker, A.K., Riishuus, M.S., Andreasen, R., 2008. Temporal variations in crustal assimilation of magma suites in the East Greenland flood basalt province: Tracking the evolution of magmatic plumbing systems. Lithos 102, 179–197.
Puchtel, I.S., Mundl-Petermeier, A., Horan, M., Hanski, E.J., Blichert-Toft, J., Walker, R. J., 2020. Ultra-depleted 2.05 Ga komatiites of Finnish Lapland: Products of grainy late accretion or core-mantle interaction? Chem. Geol. 554, 119801.
Robertson, J., Ripley, E.M., Barnes, S.J., Li, C., 2015. Sulfur liberation from country rocks and incorporation in mafic magmas. Econ. Geol. 110, 1111–1123.
Romer, R.L., 1996. U-Pb systematics of stilbite-bearing low-temperature mineral assemblages from the Malmberget iron ore, northern Sweden. Geochim. Cosmochim. Acta 60, 1951–1961.
Santaguida, F., Luolavirta, K., Lappalainen, M., Ylinen, J., Voipio, T., Jones, S., 2015. The Kevitsa Ni-Cu-PGE Deposit in the Central Lapland Greenstone Belt in Finland. In: Maier, W.D., Lahtinen, R., O'Brien, H. (Eds.), Mineral Deposits of Finland, First ed. Elsevier, Amsterdam, Netherland, pp. 195–210.
Scoates, J.S., Friedman, R.M., 2008. Precise Age of the Platiniferous Merensky Reef, Bushveld Complex, South Africa, By The U-Pb Zircon Chemical Abrasion ID-TIMS Technique. Econ. Geol. 103, 465–471.
Skaar, J.A.A., 2014. 3D geophysical and geological modelling of the Karasjok Greenstone Belt. Norwegian University of Science and Technology, NTNU, Department of Geoscience and Petroleum, p. 158.
Stokmo, E.B., 2020. Superimposed macro- and mesoscale folds, and their relation to ductile shear zones in the Karasjok Greenstone Belt. UiT The Arctic University of Norway, UiT, Finnmark, Norway, Department Of Geosciences, p. 61.
Sun, S.S., McDonough, W.F., 1989. Chemical and isotopic systematics of oceanic basalts: implications for mantle composition and processes. Geological Society, London, Special Publications 42, 313–345.
Wall, C.J., Scoates, J.S., Weis, D., Friedman, R.M., Amini, M., Meurer, W.P., 2018. The Stillwater Complex: Integrating Zircon Geochronological and Geochemical Constraints on the Age, Emplacement History and Crystallization of a Large, Open-System Layered Intrusion. J. Petrol. 59, 153–190.
Weaver, B.L., Tarney, J., 1984. Empirical approach to estimating the composition of the continental crust. Nature 310, 575–577.
Wilson, A.H., Zeh, A., Gerdes, A., 2017. In Situ Sr isotopes in Plagioclase and Trace Element Systematics in the Lowest Part of the Eastern Bushveld Complex: Dynamic Processes in an Evolving Magma Chamber. J. Petrol. 58, 327–360.
Yang, S.-H., Maier, W.D., Hanski, E.J., Lappalainen, M., Santaguida, F., Määttä, S., 2013. Origin of ultra-nickeliferous olivine in the Kevitsa Ni–Cu–PGE-mineralized intrusion, northern Finland. Contrib. Miner. Petrol. 166, 81–95.
Yudovskaya, M.A., Naldrett, A.J., Woolfe, J.A.S., Costin, G., Kinnaird, J.A., 2015. Reverse Compositional Zoning in the Uitkomst Chromitites as an Indication of Crystallization in a Magmatic Conduit. J. Petrol. 56, 2373–2394.